First Edition

# Nuclear Magnetic Moments

Gerfried Kumbartzki
2015

---

## Guide to transient field experiments

# Guide to Transient Field Experiments

**Magnetic properties of nuclei play an important part in the understanding of nuclear structure. They also tell us about the contributions of protons and neutrons to the wave functions of excited nuclear states.**

# Magnetic Moments

## Introduction

What do magnetic properties tell us about nuclei? Nuclei are made up of protons and neutrons held together by the strong nuclear force. Protons have a positive charge of one. The Coulomb repulsion in heavier nuclei is overcome by a surplus of neutrons. For instance lead, mass 208, has 82 protons and 126 neutrons.

Only a narrow band of proton-neutron combinations results in stable nuclei, depicted in the chart of nuclei as black squares.

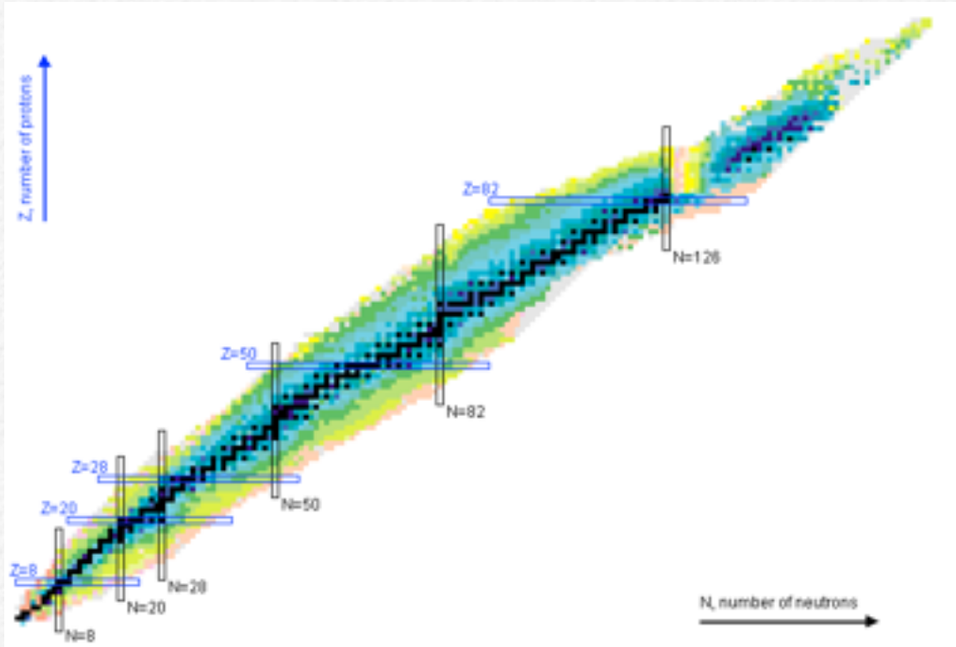


Chart of nuclides

The nucleus is a finite quantum system of spin 1/2 particles (fermions) and the pecking order of the nucleons is governed by the Pauli exclusion principle; no two fermions can occupy the same state simultaneously.

Nucleons in the confines of a nucleus (r ~ $10^{-15}$m) have high kinetic energies (uncertainty principle), that is they move around at relativistic speeds. Still nuclei exist in unique stable states, e.g. all $^{12}C$ nuclei are the same, excite to the same states. The idea is the nucleons can only exist in a given set of orbits, where they form “standing waves” with increasing numbers of nodes, which are the basis for the shell model, following very much the Bohr model of the atom.

Protons have a charge, therefore protons ‘moving’ in orbits give rise to an orbital magnetic moment.

The nucleons, protons and neutrons, have spin and the spin angular momentum also gives rise to a magnetic moment.

Classical physics predicts the magnetic dipole moment μ for a body with a charge q and a mass m rotating around a symmetry axis with an angular momentum mvr = L to be

$$\mu = \frac{q}{2m} \cdot L$$

This relation should also hold for the spin angular momentum. A charged particle with a spin has a magnetic moment, but its value differs from the classical by a dimensionless factor, the *g* factor:

$$\mu = g \cdot \frac{e}{2m} \cdot S$$

Like the magnetic moment of an electron the “spinning” proton should come with a magnetic dipole moment and have $g = 2$. When measured, protons and neutrons (no charge!) had larger *g* factors than expected from theory, which is attributed to their internal structure of three quarks.

Proton: $g_s = +5.5856912(22)$ $g_l = +1$

Neutron: $g_s = -3.8260837(18)$ $g_l = 0$

In nuclei, due to the strong pairing force, alike nucleons with opposite spin couple to angular momentum zero. All even-even nuclei have spin $I = 0$ in their ground state and no magnetic moment

$$\mu = g_I I \mu_N / \hbar.$$

The unit is the nuclear magneton $\mu_N = \frac{e\hbar}{2m_p}$ with $m_p$ the proton mass.

For other nuclei the ground state magnetic moment is determined by the last odd nucleon. Which leads to the Schmidt values [SCH37].

The Schmidt limits are given for protons and neutrons separately for j = l + (1/2) and j = l - (1/2). Experimental *g*-factor val-

ues fall within these limits. Good agreement between calculated and measured magnetic moments is obtained when the spin part of the *g* factor is reduced to an effective $g_s^{\text{eff}} \simeq 0.7 g_s^{\text{free}}$. This observation suggests that other effects inside the nucleus, like meson exchange currents, contribute to the total magnetic moments.

Because of the characteristic differences of the sign and size of the *g* factors for protons and neutrons, the magnetic moment of a state is sensitive to the single-particle structure and therefore to the contributions of protons and neutrons to the wave function of the state.

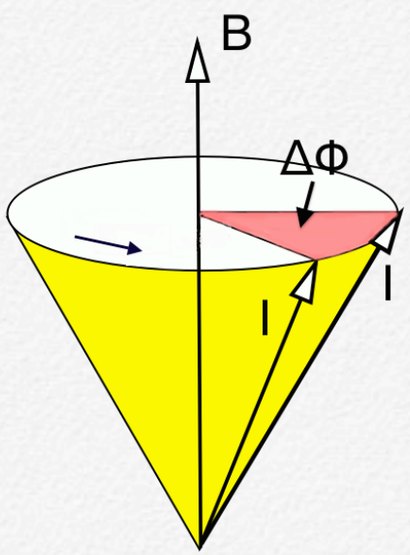


This treatise is about measuring magnetic moments of excited states. Prerequisite is an ensemble of spin aligned nuclei in a magnetic field.

Magnetic Moments are measured by subjecting the excited nucleus to an external magnetic field and observing the Larmor precession of the nuclear spin

$$\omega_{\text{Larmor}} = \frac{d\theta}{dt} = g\frac{e}{2m_p}B$$

In a given time **t** the spin **I** will precess by an angle **ΔΦ**:

$$\Delta\phi = -\frac{\mu_N}{\hbar} gBt \qquad (1)$$

Aligned nuclei radiate their energy anisotropically and the precession angle is determined from the rotation of the angular distribution of the decay $\gamma$ rays.

This method is known as PAC (perturbed angular correlation) measurement. When the precession is taken over the whole lifetime of the excited state the method is called IPAC (integral perturbed angular correlation).

Practical measurements require precession angles of a few milliradians (1rad = 360°/2π = 57.296°). If the life time of the excited state, for instance a first $2^+$ state in an even-even nucleus, is of the order of 1 picosecond (1 ps = $10^{-12}$s, the time light travels 0.3mm), a simple estimate using equation (1) shows, that for a measurable effect magnetic fields in the range of kilotesla (kT) will be needed. For comparison, the earth's magnetic field is about 50 μT, a LHC superconducting magnet is 8 T and a saturated iron electromagnet tops out at 2 T.

Kilotesla fields exist. They exist as inner atomic or hyperfine fields.

# Transient field

## Introduction

Transient fields were discovered in 1967, accidentally, when ions were implanted into a ferromagnetic lattice to make use of its strong internal field for measuring magnetic moments.

Online, a small precession was seen before the ions came to rest. This effect was attributed to what was then named *transient field.* It was also speculated, that the fields are hyperfine fields, fields originating in atoms caused by their own electrons.

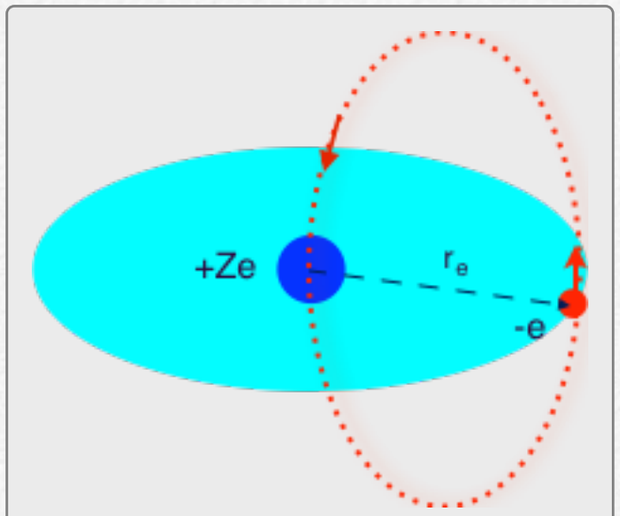


FIGURE
Guide to Transient Field Ex
.1
Bohr model of a hydrogen-like atom.

In the classical picture

$$\frac{m_e v^2}{r_e} = \frac{Ze^2}{r_e^2}$$

the Coulomb force is equal to the “centripetal force”. If combined with the quantization of the angular momentum, only orbits are allowed for which

$$mvr = n\hbar \qquad (n=1,2,3,...)$$

From these 2 formula $r$ and $v$ are derived to be

$$r_n = \frac{n^2\hbar^2}{m_e Z e^2} \quad \text{and} \quad v_n = \frac{Ze^2}{n\hbar}$$

Using the fine structure constant $\alpha = \frac{e^2}{\hbar c} = 1/137.036$ and the Bohr velocity $v_0 = \frac{e^2}{\hbar}$ (velocity of the electron in the ground state of the hydrogen atom) the expressions reduce to

$$r_n = \frac{n^2\hbar}{Z m_e \alpha c} \quad \text{and} \quad v_n = \frac{Zv_0}{n}$$

Take notice of the dependence on *n*, the principle quantum number.

## Hyperfine fields

The hyperfine structure in atomic transitions is caused by the magnetic interaction of the magnetic moment of the nucleus with its electrons. The electrons surrounding the nucleus create the hyperfine field. In general the hyperfine field $B_{\text{hf}}$ at a nucleus of an atom is made up mainly of three parts

$$B_{\text{hf}} = B_{\text{Fermi}} + B_{\text{orbital}} + B_{\text{spin}}$$

where:

- $B_{\text{Fermi}}$ is the Fermi contact term, which is related to the direct interaction of the nuclear magnetic dipole moment with the electron spin dipole moments and is only non-zero for states with a finite electron spin density at the position of the nucleus, as in atoms with unpaired electrons in s-orbitals.
- $B_{\text{orbital}}$ is the field due to the electrons`s orbital angular momenta.
- $B_{\text{spin}}$ is the field due to the electron`s spin magnetic moments

See Figure 1.

The largest contribution comes from $B_{\text{Fermi}}$ of an unpaired s electron in an atom.

$$B_{\text{ns}} = 16.7 \cdot R(Z) \cdot (\frac{Z}{n})^3 \quad \text{[Tesla]}$$

where $R(Z) = 1 + (Z/84)^{(5/2)}$ is a relativistic correction.

For hydrogen (Z = 1) $B_{1s} = 16.7$ T. Uranium (Z = 92) would have a $B_{1s} = 29.3$ MT.

These fields have a **sign** which is related to the spin direction of the electrons. Only when there is a spin polarization can we expect a net field direction.

With these assumptions the observable transient field strength maybe expressed as a sum of many contributions

$$B_{TF} = \sum_n q_{\text{n}}(Z, \text{v}_{\text{ion}}) \cdot p_{\text{n}}(Z, \text{v}_{\text{ion}}, \text{Host}) \cdot B_{\text{ns}}(Z)$$

where

- n are the principle quantum numbers, 1, 2, 3,...
- $q_{\text{n}}(Z, \text{v})$ the charge state distributions of the ions
- $p_{\text{n}}(Z, \text{v,Host})$ the degree of polarization of the electron spins
- $B_{\text{ns}}(Z)$ Hyperfine field ( $\sim Z/n)^3$ )

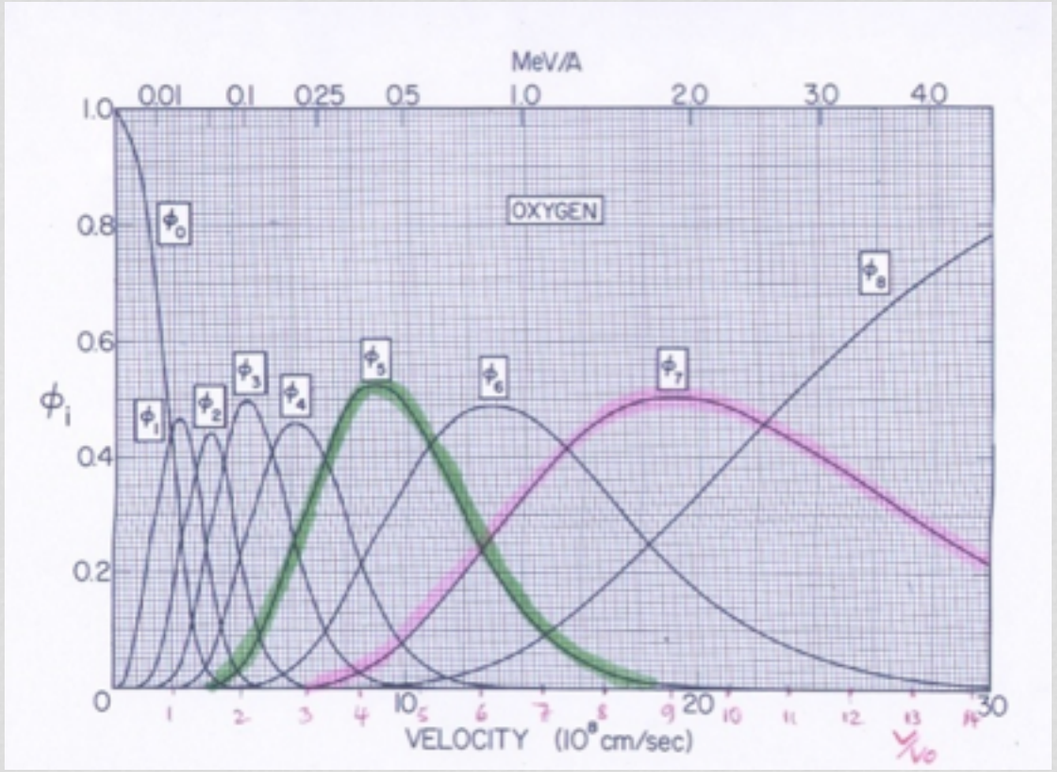


FIGURE Guide to Transient Field Experiments.2

Charge state distributions of oxygen atoms after leaving from a foil into a vacuum. Highlighted are the 1s and 2s distributions (The figure is taken from Marion and Young [MA68]).

implying the major contribution comes from single electrons in s orbits.

Charge state distributions of ions moving inside a solid are not known. For ions exiting foils data were measured and the charge state distribution can be calculated.

Figure 2 is an example for oxygen ions emerging from a carbon foil.

The velocity scale as shown in Figure 2 should be different inside the solid medium. A common assumption is that the maximum of the 1s charge state distribution occurs at $v \sim Z \cdot v_o$. The curves of Figure 2 have to be rescaled accordingly to peak at lower velocities.

The polarization $p_n$ in the expression oft $B_{TF}$ is the least understood part. As a matter of fact, a polarization of electron spins is observed, when ions move in a polarized ferromagnetic host (iron, gadolinium). When the direction of the magnetizing field is changed, the net field direction of the transient field changes accordingly.

As stated in the original paper by Borchers et al. [BO68] the transient field is always positive.

> "The spin of a polarized electron in an iron lattice is opposite in direction to the external magnetizing field and those electrons are probably most often picked up without spin flip... The field at the nucleus due to s electrons is opposite to the spin direction; hence *H* is in the direction of the aligning field, i.e, positive."

They also observed:

> "The transient field is roughly proportional to the concentration of polarized electrons in the conduction band of the host."

The exact charge state distributions of ions traversing the ferromagnetic layer, their state of excitation or degree of polarization and how the polarization transfer from the medium to the moving ions is facilitated (electron capture and loss, spin-spin scattering) are all still not known. However, using known *g* factors, the *Z* (charge) and *v* (velocity) dependences of the field strength were measured and parametrized. A quantitative or microscopic description of the observed field strength is still outstanding.

### Historical Note

Shortly, after the discovery of the transient field, Lindhard and Winter [LW71] described the phenomenon as due not to hyperfine interactions but due to a spin-density enhancement near the moving ions. The moving ion attracts electrons from the surrounding polarized ferromagnetic host. This theory predicted the field strength to vanish with higher velocities. Only later, when using the transient field to determine the sign of the *g* factor in $^{18}$O, it was found that the field actually increases substantially with the ion velocity.

## Transient Field Parametrization

The transient fields had to be calibrated. There were g factors known from measurements with internal fields which could potentially be used for calibration. An average B can be obtained from a measured precession angle using the equation 1. and the known *g* factor. (See also later in Chapter 1, Section 5).

Early on it was recognized that the transient field strength was varying smoothly with the ion velocity and ion species. The simplest approach was, of course, the assumption of a linear dependence on Z and v. That was supported at the beginning by measurements with light ions and relatively low velocities [EB77]. It was soon realized, however, that the linear parametrization was too simple. Later, for heavier ions and higher velocities, smaller fields were needed to describe the data and an attenuation factor *G* was postulated:

$$B_{\mathrm{TF}} = a \cdot G_{\mathrm{beam}} \cdot Z \cdot (\mathrm{v}/\mathrm{v_o})$$

This attenuation factor *G* depends on the mass of the beam projectiles, on $dE/dx$ of the beam in the ferromagnet and on the charge state of the probe ions [Sp89]. It is an empirical factor and cannot be derived from first principles. The common expla-

nation for it is an unspecified loss of magnetization of the ferromagnet in beam. The coefficient $a$ is a fit parameter and was found to be different for gadolinium and iron hosts.

Already in 1980 a group from Rutgers published another parametrization:

$$B_{\mathrm{TF}} = 96.7 \cdot Z^{1.1}(\frac{v}{v_0})^{0.45} \cdot M \qquad (2)$$

This parametrization was derived from a fit of measured transient field precession data for a limited number of nuclei with known *g* factors ranging from O to Sm in a velocity range between 2 $v_o$ and 4 $v_o$. On the next page is the relevant figure from the original publication by N.K.B.Shu et al. .

Noticeable is the inclusion of the magnetization *M* of the ferromagnetic foil. $M = \mu_B \cdot N_p$ where $\mu_B$ is the Bohr magneton and $N_p$ is the volume density of polarized electrons in the ferromagnet. In the data the horizontal 'error' bars represent the velocity range of the probe ions, as they move into and out of the ferromagnetic foil.

The fit came with large uncertainties in the exponents for Z (1.1 ± 0.2) and v/$v_o$ (0.45 ± 0.18), uncertainties which are usually not included in the application of the parametrization. There is also an uncertainty in the strength parameter 96.7(16). Overall,

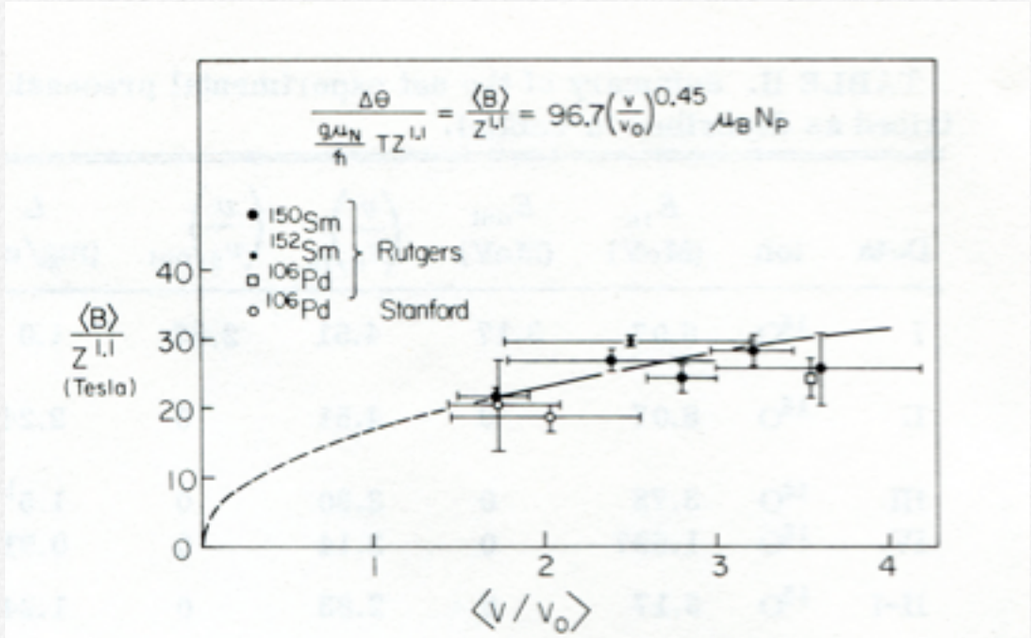


FIG. 5. Plot of the average value of the dynamic field $\langle B\rangle$ versus the transit velocity of Sm ions traversing iron foils. The solid line is a representation of the dynamic field according to Eq. (4) and the dotted line indicates the region where the formulation for Eq. (4) need not apply as no experimental data are available.

a 10% error should be assumed in precession calculations using this parametrization.

No distinction in the parametrization is made for iron versus gadolinium. The underlying assumption comes from the finding that the field strength is proportional to the available volume magnetization (density of polarized electrons). It just happens, that the volume density of polarized electrons in iron and gadolinium is similar. Let's look at the numbers: Iron has 2.2 polar-

ized electrons per atom while gadolinium has 7.6. And 55.8 g of iron and 157.2 g of gadolinium have the same number of atoms (1 mole). The density, $\rho = 7.9$ g/cm$^3$ , is the same for both. The full magnetization of gadolinium is 0.2116 T while for iron it is 0.1706 T. Iron foils are usually fully magnetized, while typical gadolinium foils have only a magnetization of 0.1700 - 0.1800 T, just about the same as fully magnetized iron. In the calculation of the field strength, therefore, the measured magnetizations are applied regardless of the specific ferromagnet.

The Rutgers parametrization is not expected to represent the data on light ions and high velocities. The parametrization also was not based on the idea that the transient field is basically a hyperfine field and follows the charge state distribution as it was shown earlier in measurements on carbon.

A different presentation of the data is offered by replacing the explicit v dependence with $v/(Z \cdot v_o)$. This puts the v dependence of the field strength solely into the charge state distribution as it applies to 1s configurations. Although, the orbital velocities of the higher n orbits are lower (divided by n) and the approach ignores any v dependence of the polarization. Since the transient field is a sum of averaged quantities, there are no clear separations in the data between 1s, 2s, and higher configurations. The linear increase of $B_{TF}$ with $Z$ and the scaling with the magnetization $M$ are preserved.

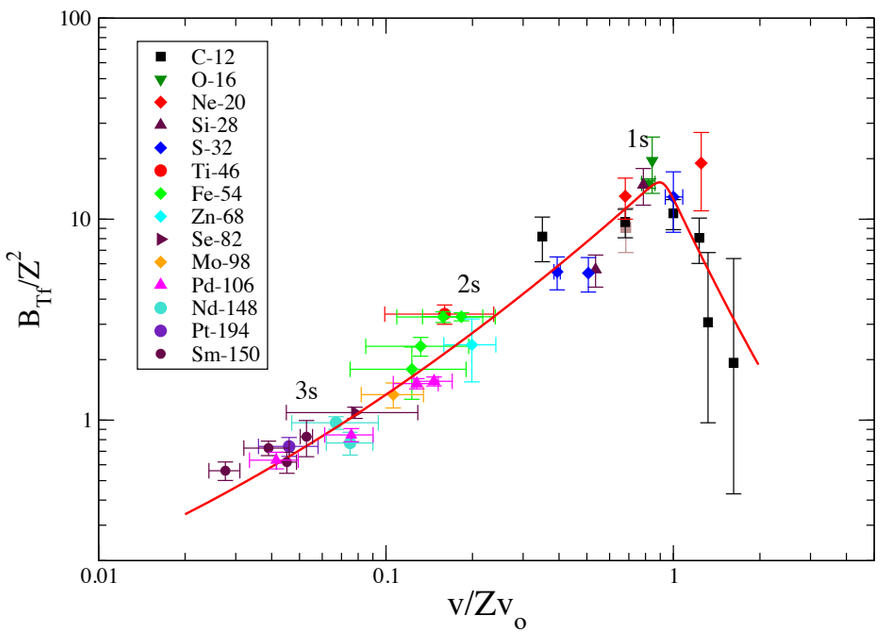


FIGURE Guide to Transient Field Experiments.3
Transient field calibration data using previously measured *g* factors.

Figure 3 is a contemporary compilation of transient field measurements for nuclear states with known *g* factors. These calibration points have individual errors up to 30 % and therefore any transient field parametrization taken as absolute field calibration is at best an average with an uncertainty of the order of 10% .

Often therefore, instead of the parametrization, known *g* factors of nearby nuclei ($Z \pm 2$), measured under similar kinematic

conditions, are used for calibration. This method of course defies the averaging effect of the parametrization.

The uncertainties of the parametrization cancel out when relative *g* factors in an isotopic chain are measured under close to identical kinematic conditions.

In the presentation of Figure 3 at velocities above $v/Zv_o = 1$ the maximum of the 1s charge state distribution is exceeded and the field strength falls off, in agreement with having no hyperfine field for bare ions.

The data in the log-log plot were fitted with a seven parameter formula, which is similar to the expression usually used for the presentation of the relative efficiency of Ge detectors. Each "straight" part is represented by an expression of the form $a + b \cdot x + c \cdot x^2$ where $x$ is $\log(v/Zv_o)$ .

$$B_{TF} = \exp[(a + b \cdot x + c \cdot x^2)^{-g} + (d + e \cdot x + f \cdot x^2)^{-g}]^{-1/g}$$

The parameters for the fit of Fig. 4 are

- $a = 2.92(6)$
- $b = 1.31(9)$
- $c = 0.074(30)$
- $d = 2.56(13)$
- $e = -3.78(76)$
- $f = 2.64(98)$
- $g = 13.57(100)$

(This part is still work in progress.)

CHAPTER 1

# Experiment

**Sections**

1. **Target**
2. **Magnets**
3. **Detectors**
4. **Angular Correlations**
5. **Precession measurements**

SECTION 1

# Target

The center piece for a transient field experiment is a multi-layer target. The nuclei of interest, also called probe ions, are created in the first layer; the nuclei are excited, spin-aligned and ejected with a certain velocity forward out of the target layer. The second layer is a ferromagnetic substance. The probe ions should have enough velocity to traverse this layer. And finally, the ferromagnetic layer should be backed by a material which stops the probe ions in a field free (no internal fields) environment.

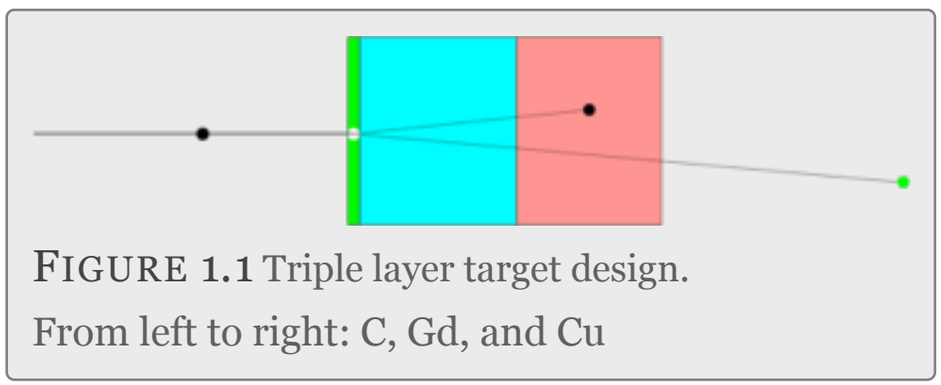

FIGURE 1.1 Triple layer target design. From left to right: C, Gd, and Cu

In early experiments the first layer was the substance to be investigated, often a thin layer of an enriched isotope or a mixture of several isotopes. Beams of light ions were used to excite nuclei and impart sufficient energy to 'recoil' the nuclei forward out of the target and through the ferromagnetic layer.

In this conventional kinematics condition the backwards scattered beam particles were detected in a ring detector covering a typical solid angle range between 170° - 150°.

The availability of mono-isotopic beams accelerated to several 100 MeV opened the way to study ions provided as beam projectiles. A light first-layer target material, e.g. carbon, became the choice of a 'standard' target (Figure 1.1). Under this inverse kinematics condition, where the projectiles are heavier than the target nuclei, the excited beam projectiles and the knock-on target nuclei move forward and pass through the ferromagnetic layer with high speed. While the excited probe ions will be stopped in the target backing, the light nuclei escape and are detected in a particle detector placed beyond the target at 0° to the beam.

The ferromagnetic layer, iron or gadolinium, should be thick enough to allow the transient field to act long enough to produce a measurable spin precession, but also thin enough to let the probe ions pass. Although gadolinium is a much more difficult material to handle and its Curie temperature is low, it is preferred, since it has a higher $Z$ and therefore the ions lose less energy per distance travelled. Thus thicker gadolinium layers can be used. It was also assumed that gadolinium,

with more polarized electrons, should give larger effects. Later it is shown that that is not the case.

A typical ferromagnetic layer is a few µm (micrometer, micron) thick. For comparison, the diameter of a human hair is 50 - 70 µm. These thin foils have to be prepared to have good magnetic properties. Rolled foils have to be annealed at high temperatures without oxidation. The surfaces have to be clean to assure good adherence of the front and back layers of the target.

As target backing materials with simple crystal structure like Al, Cu, Ag and Au can be used. They provide a field free  environment where the stopped ions decay without further reorientation of spins.

The target making starts with the preparation of the ferromagnetic foil followed by the evaporation of the backing material. It is difficult to add sufficiently thick carbon by evaporation. Carbon does not adhere well and tends to detach, roll ‘off’ from the iron or gadolinium because of its high surface tension. A few µg/cm² of a buffer material (Ti or Cu) were tried to improve the adherence of the carbon. Also carbon was sputtered on with moderate success (cracked in beam). A less precise method is painting the target with a liquid colloidal suspension of graphite in alcohol or water (look for Aquadag). Evaporated layers are typically less than 0.5 mg/cm². The graphite solution was used to make layers of more than 1 mg/cm² by applying several coats.

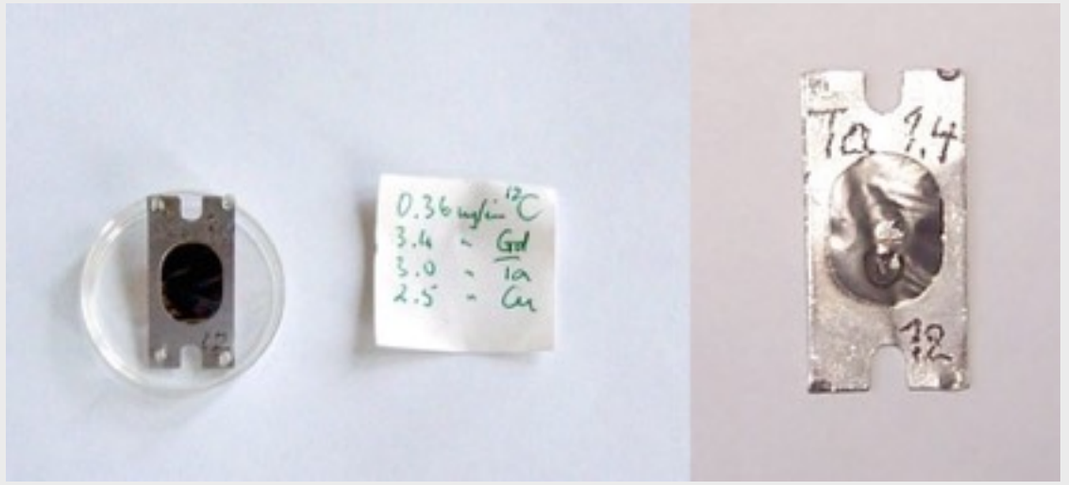


FIGURE 1.2 Sample targets.
The right target shows a typical beam spot.

Section 2

# Ferromagnets



## Iron

In conventional kinematics experiments the recoil velocities of probe ions were limited to 2 - 4 $v_o$, This puts a limit on the foil thickness.

Target thicknesses are usually given in mass per area (mg/cm$^2$). Knowing the density of a material ρ, that is the weight of 1 cm$^3$ in grams, a useful relation to remember is:

the value of ρ in mg/cm$^2$ = 10 µm thick.

With $\rho = 7.87 g/cm^3$, the density of iron, $3 mg/cm^2 \sim 2.4\ \mu m.$

For instance, such a foil would be considered already as “too thick” for a Coulomb excitation experiment with a sulfur beam of 80 MeV on a Pt target. The recoil energy of the Pt ions into the Fe layer would be about 36 MeV and the energy loss in 3 mg/cm$^2$ is 26 MeV. The exit velocity is only 1.44 $v/v_o$ .

On the plus side, iron is relative easy to polarize, aligning all magnetic domains in a sample. The saturation magnetization is 0.1706 T and the Curie temperature is 770 °C (1043 K). Iron targets can be used at room temperature.

Iron as ferromagnet should be considered, with high velocity beam projectiles. The power deposition by heavy ion beams of several 100 MeV and currents of a few $10^{-9}$ A in the target becomes a major concern. Iron with the higher Curie temperature has then an advantage compared to gadolinium.

# Gadolinium

Most experiments so far used Gd as ferromagnet. Compared to Fe, the ions lose only half the energy while traversing the same layer thickness. The density of Gd, $\rho = 7.9 mg/cm^2$, is the "same" as for Fe. Instead of 2 µm iron 4 µm gadolinium can be used for the same energy loss (velocity range).

The preparation of Gd foils with good magnetic properties is tricky. Rolling destroys the crystal structure and requires careful annealing. Gd oxidizes easily and thin foils can combust spontaneously. Therefore, for rolling, some samples were covered with "messy" oil. Rolling can also introduce pin holes. Often such foils have poor magnetic properties.

At the Technische Universität in Munich, Germany, a method was developed to evaporate Gd on a high temperature Ta substrate (~ 1.0 mg/cm$^2$). Layer thicknesses up to 8 mg/cm$^2$ with magnetizations of 80% of 0.2116 T, the theoretical saturation magnetization, were routinely obtained.

The Curie temperature of Gd is 292 K (19 °C). Fig. 1.3 shows the measured magnetization as function of the temperature for one of the Munich targets. Gadolinium targets have to be cooled. The beam-spot temperature has to be kept below 150 K with beam applied. Beam heating of the target and a corresponding loss of magnetization has to be carefully considered. Gd is a very poor heat conductor. The heat dissipation in vacuum is mainly due to radiation. So far, a defocused low-intensity beam is the best way to keep the temperature of the target spot below the 150 K necessary for preserving the magnetization.

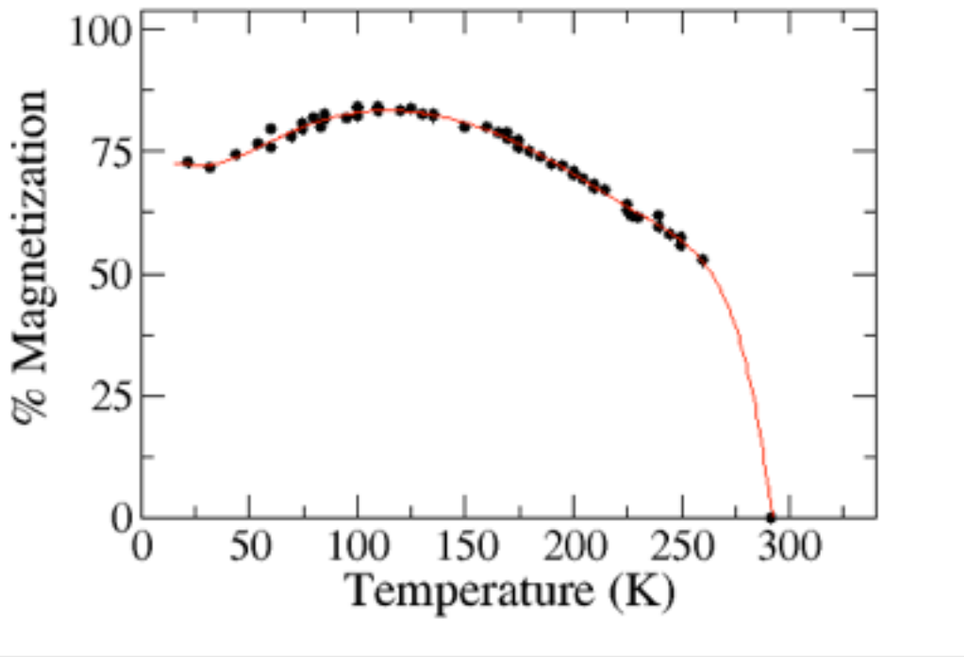


FIGURE 1.3 Magnetization of a 6 mg/cm$^2$ gadolinium foil. The full magnetization is 0.2116 T.

Reality is, the target spot temperature is not known in current experiments and therefore the magnetization is essentially unknown. Unfortunately, no monitor or device for measuring the beam-spot temperature exists at this time. With modern infrared techniques such a system should be developed.

## Magnetometer

The magnetization of the targets is measured *offline*. After exposure to the beam, repeat measurements showed no deterioration of the magnetic properties in a target.

A 60 Hertz *ac* magnetometer was designed to measure magnetizations of samples of few milligrams, as functions of temperature and applied magnetic fields [PI89].

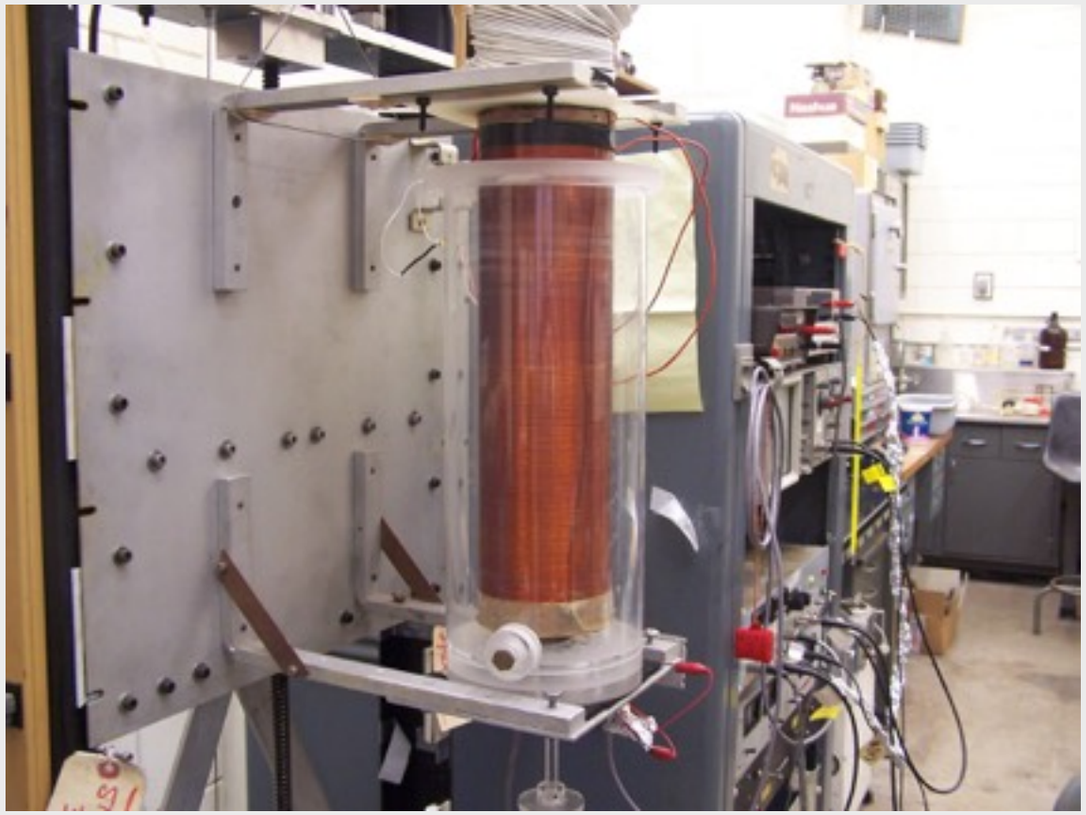

FIGURE 1.4 Rutgers Magnetometer

The driver coil has to be cooled. The sample is introduced from the bottom. In fact the whole coil assembly is moved up and down. Samples can be cooled down to 12 K.

## Sample Magnets

Liquid nitrogen (LN) cooling is used in the design depicted in Fig. 1.5. The coil of the magnet is submerged in the LN bath fed from above with a “chicken feed” dewar.

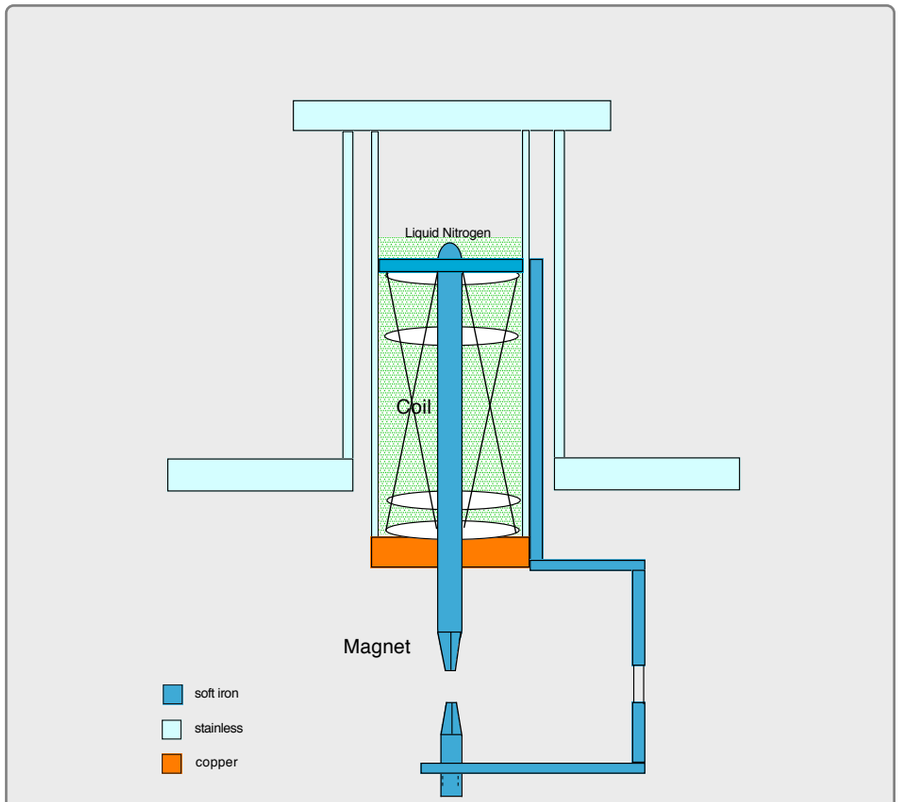


FIGURE 1.5 LN cooled magnet.

The target is mounted between the pole tips. The beam enters from the right through the hole in the return yoke. The stainless steel part is the lid of the vacuum chamber.

A different design uses a He-cooled Closed-Cycle Cryocooler. The top pole piece of the magnet holding the target is part of the cold tip. Target temperatures are set usually below 50 K.

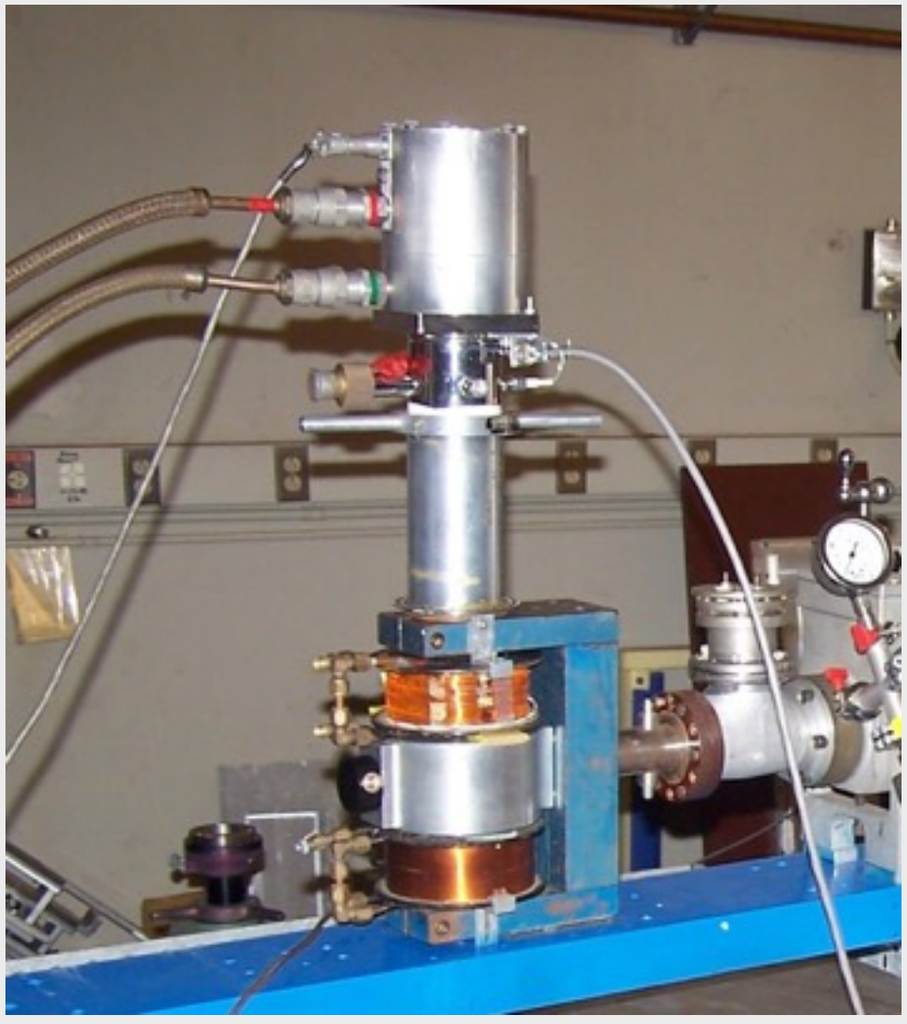

FIGURE 1.6 Cryocooler assembly

The magnetic field required to fully polarize the target depends on the sample. A typical field of 0.06 T is sufficient for most targets.  The direction of the magnetic field is reversed periodically, at intervals short compared to changes in the beam delivery. A typical field-flip time is a few minutes. The stray magnetic fields act on charged particles, the incoming beam and the scattered particles. The changing of the field direction can produce effects which simulate a precession effect. Therefore, the fringe field of the magnet should be minimized (shape of pole pieces) and shielding cones of soft iron and/or Mu-metal can be employed around the incoming beam path and the path to the particle detector (Fig. 1.7).

Measured “beam bending” effects were always negligibly small and thus are usually ignored.

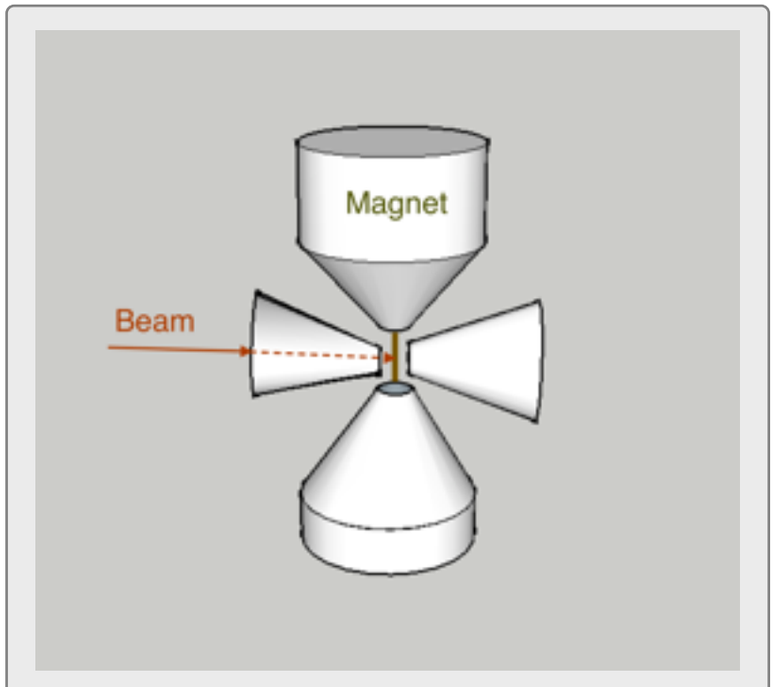


FIGURE 1.7 Sketch of magnetic shields for the incoming beam and outgoing particles

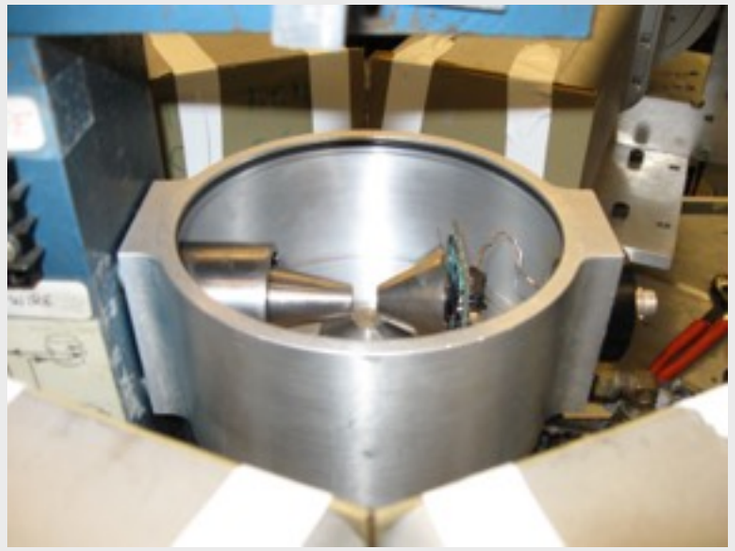

FIGURE 1.8 Implementation of shielding cones. The beam enters from the left and is stopped before the particle detector on the right side,

# Detectors

## Particle detection

Particle detection is important for the selection of the reaction products. The kinematics of the reaction products, like the scattering angle and energy of particles, determine the properties of the probe ions, their energy and spin alignment. The coincidence detection of scattered particles and decay-$\gamma$ rays of the excited probe ions selects the reaction products and their angular correlation.

In conventional kinematics experiments the particle detector is typically an annular Si surface-barrier detector. The beam passes through the center hole and the back scattered beam projectiles are recorded. The finite opening angle of the detector restricts the kinematic range of the forward scattered probe ions and their alignment, which directly affects the particle-$\gamma$ angular correlation.

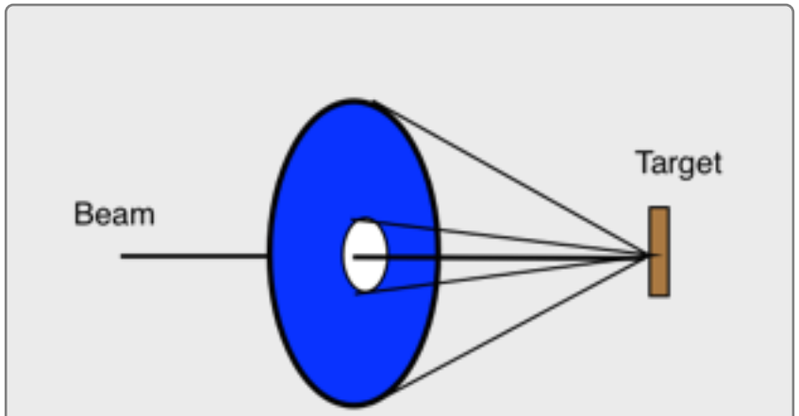


FIGURE 1.9 Annular detector upstream of the target as used in a conventional kinematics experiment.

In inverse kinematics all particles of the reaction move forwards in the lab system. The forward scattering cone of the excited projectiles depends solely on the masses of projectile and target nuclei and is only a few degrees wide. The light target nuclei can scatter up to 90° to the beam direction, but with less and less energy and intensity.

It is very important that no beam particles reach the detector. A thin beam stopper is placed between the target and the particle detector. A good rule is to have a beam stop thick enough to stop the full beam energy regardless of the target. That protects the particle detector in case of nonuniformities in the target thickness and possible pin holes.

It is recommended to place the beam stop just in front of the particle detector and to have it cover the whole detector face. This prevents other scattered particles from reaching the detector and lets the reaction particles from the target pass the fringe field of the magnet with their full energy. The beam stop has to be thin enough to let the light particle through without losing too much energy. There is a kinematic cutoff angle due to the diminished particle energy after passing through all the foils. That angle is about ± 40°(see Figure 2.3). So, it makes no sense to use detectors with larger opening angles. Using Si strip detectors also does not provide any extra information.




FIGURE 1.10 Forward placed circular detector.

The Coulomb-excitation reaction and the relatively thick targets produce forward scattered particles with a large energy spread. Therefore, the energy and angle resolution of the detectors are less important. Important is to establish the particle - $\gamma$ coincidence.

Commercial Si particle detectors are expensive and have a limited lifecycle, especially when used with “heavy” ions (anything heavier than α particles). Due to radiation damage the leakage current increases steadily and the bias voltage has to be adjusted accordingly in order to maintain the energy gain. The higher leakage current reduces the effective bias voltage at the detector which leads to a reduction of the thickness of the depletion layer. Shunting the load resistor in the preamplifier to 10 MΩ usually eliminates that problem.

A cheap alternative to Si surface-barrier detectors are solar cell devices, which come in various shapes and sizes and cost a fraction of commercial Si detectors. They are used without bias and are insensitive to defects. An edge can be




FIGURE 1.11 Solar device and PIPS detector

broken off and the detector still works fine. They can easily be cleaned.

Solar cells can be used to make detector arrays of various shapes and sizes. The whole back of a solar cell is typically a

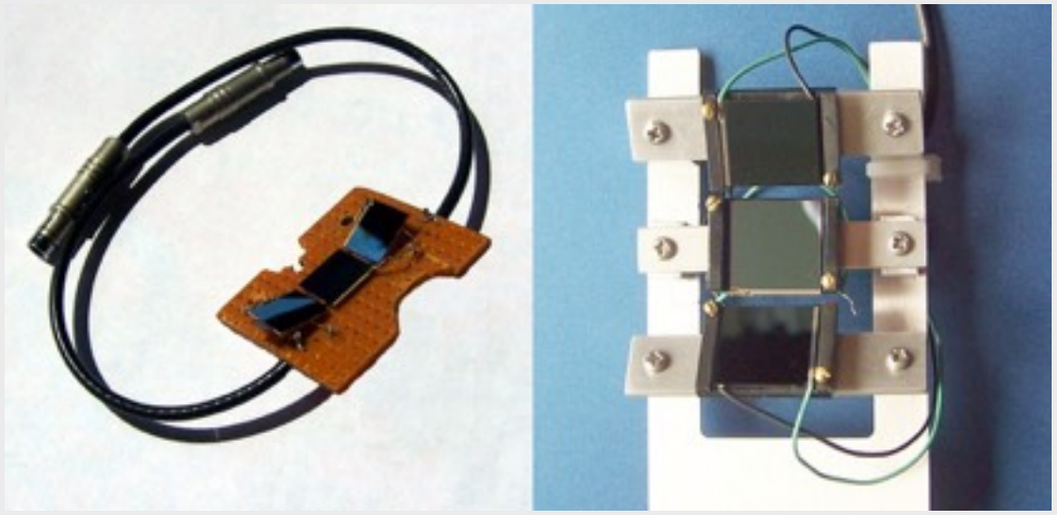

FIGURE 1.12 Solar cell detector arrays

gold contact. This contact is used to hold the cell by gluing it with a silver epoxy to a frame (ground contact). The cells come in two types of front contacts: one can be soldered, the other has to be wire bonded, which requires an expensive apparatus. Alternatively, a wire can be glued to either contact strip to make the connection.

The solar cell assembly shown in Fig. 1.12 on the right side was used at Oak Ridge National Laboratory in a $^{126}$Sn experiment.

## Gamma detection

The placement of the $\gamma$ detectors is important.

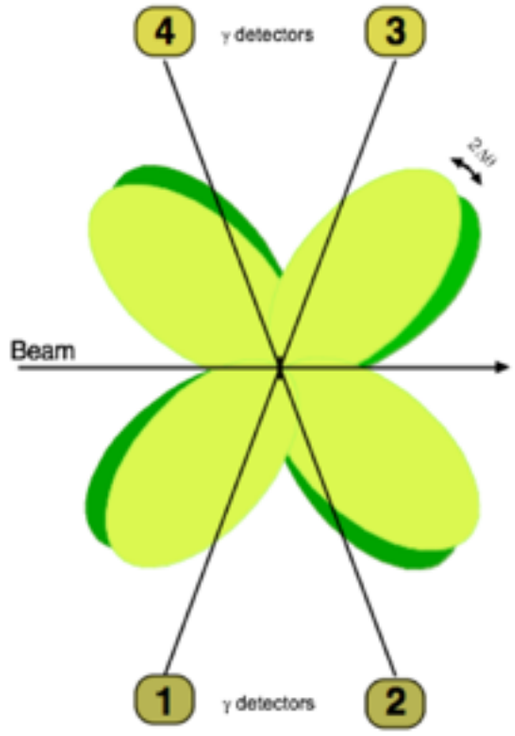


FIGURE 1.13 Idealized angular correlation of an E2 transition with a m = 0 population.

Many types of detectors were used: scintillator detectors like NaI or BaF, and Ge detectors of all types and sizes, from clover detectors to large arrays like Gammasphere. All the normal considerations like optimal size, resolution and efficiency apply.

The goal of the experiment is the measurement of a slight rotation of the angular correlation. Consider a quadrupole transition depicted in Fig. 1.13.

As shown, commonly 4 detectors mounted on an angular correlation table are used to sample the rate change when the magnetic field at the target is reversed. The magnetic field direction (which is also the direction of the transient field) is applied vertically to the detection plane of the $\gamma$ rays.

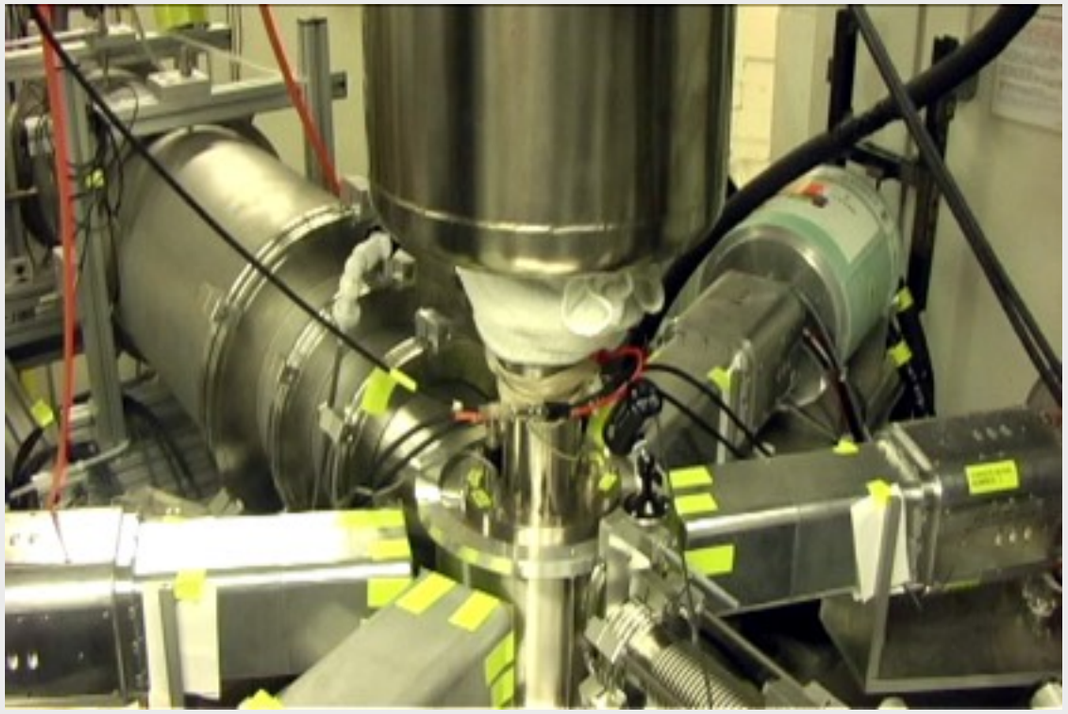

FIGURE 1.14 Clover-detector placement around the target chamber.

This setup was used at ORNL for the $^{126}$Sn experiment. In this experiment the LN cooled magnet was used.

The $\gamma$ detectors should be placed at angles where the slope of the angular correlation is large and the intensity of the $\gamma$ rays is not too low. In practice the physical constrains of the detectors used dictate their positions. They are placed as close as possible to the target to utilize their full solid angle (see Figure 1.14).

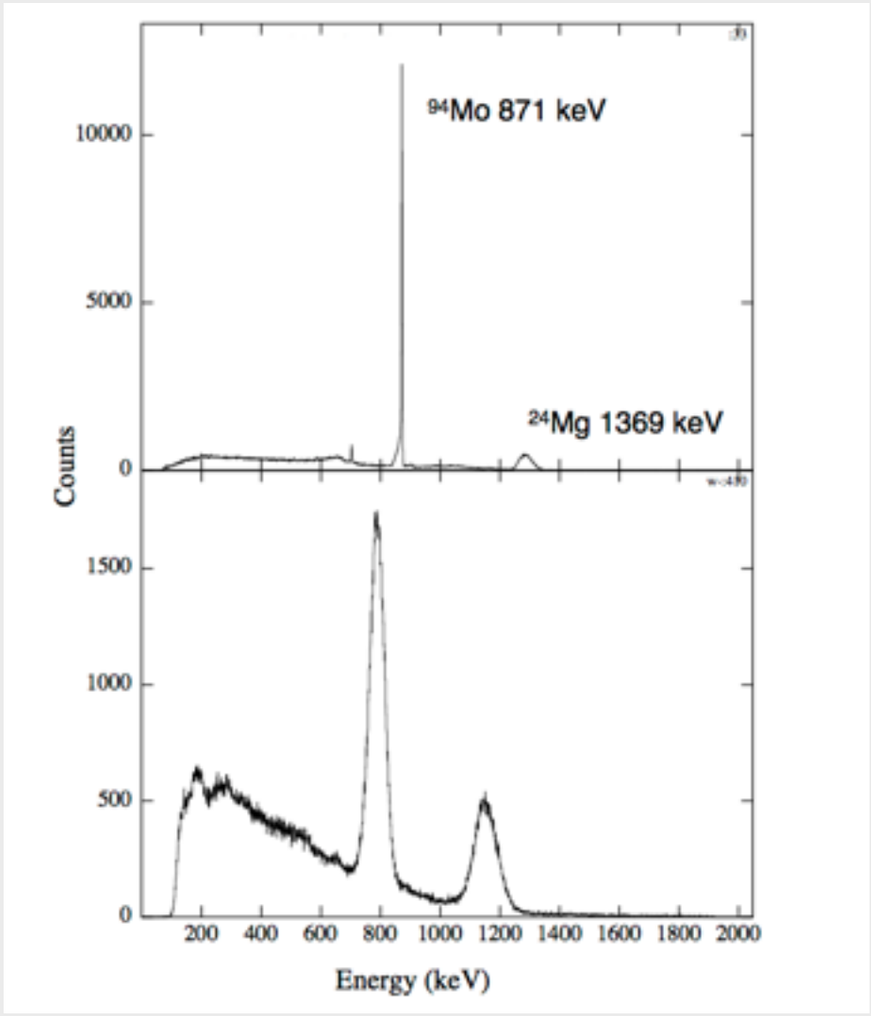


FIGURE 1.15 Clover versus 5 x 5" NaI

The molybdenum was excited on a Mg target. The top shows a clover spectrum and the bottom the corresponding NaI spectrum (slightly different energy scale). The NaI/clover efficiency ratio is 1.75 . Detector distance from target: NaI 150 mm, Clover 130 mm.

Scintillator detectors have good efficiencies and timing but lack in energy resolution. Ge detectors have low efficiency, about 25% of a 3x3” NaI, but 50 times better resolution. Clover detectors contain 4 HPGe crystals, arranged like clover leaves. Each crystal has a diameter of about 50 mm and is about 80 mm long. Due to their close proximity Compton scattered γ rays between the crystals can be added. The total efficiency including Compton add back  amounts to 150% of a 3x3” NaI detector. Relative efficiencies of Ge detectors are for historical reasons quoted in comparison to a 3x3” NaI detector, although nobody nowadays has experience with such detectors anymore.

For spectra with well separated lines, like in Fig. 1.15. the NaI detector is still a good choice. For most experiments, clover detectors are preferable. Multi-detector arrays do not add much sensitivity. Most of the detectors occupy insensitive angles and the out-of-plane detectors see a diminished anisotropy of the angular correlation. Nevertheless, they can be useful, especially when multi-coincidence requirements are needed to select a desired reaction channel.

Let us consider the application of clover detectors in more detail. Some information will also be relevant for other detector arrays.

In a 4-clover experiment a total of 16 Ge detectors are involved. Each crystal in a clover is slightly different. They differ in energy resolution and detection efficiency, which affects their exact counting response and position.

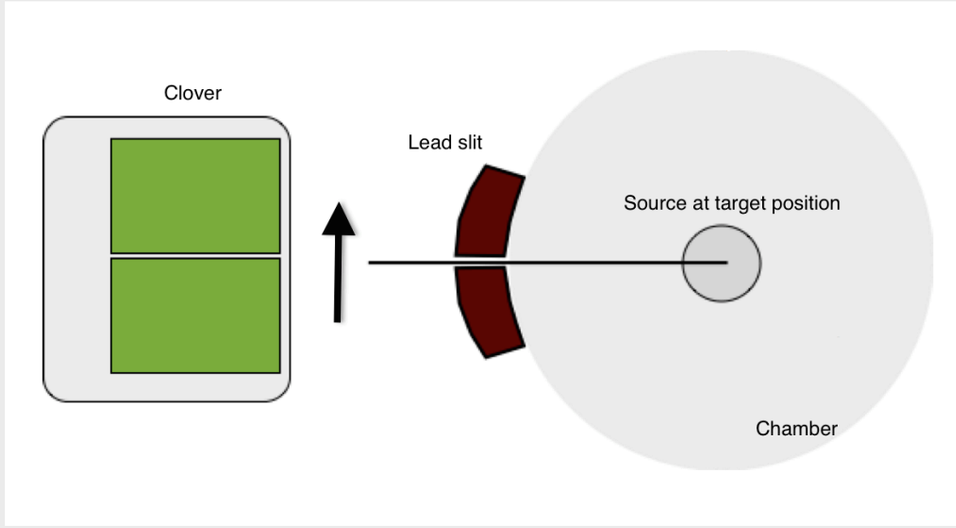


FIGURE 1.16 Detector scan arrangement

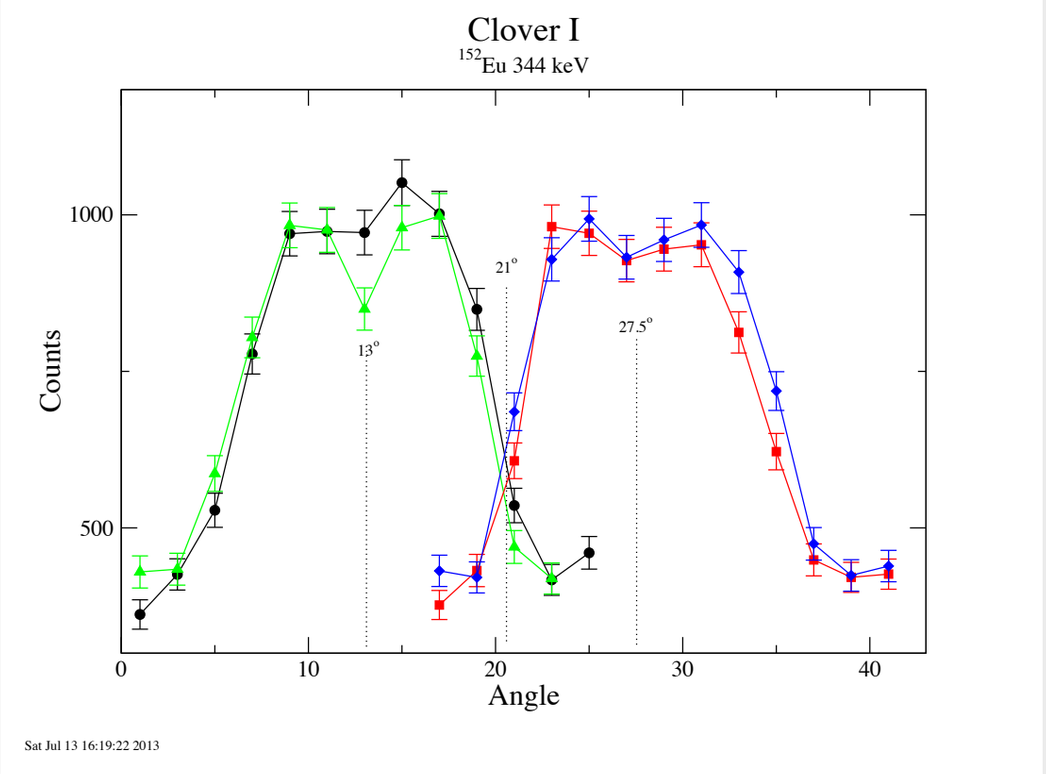


FIGURE 1.17 Horizontal scan for a clover detector

A simple setup was used to survey the response of each clover crystal. A radioactive source was placed at the target position and a lead-slit absorber was mounted at the chamber wall (Fig. 1.16). The clover detector was moved in steps of 2° across the slit. The result of the scan is shown in (Fig. 1.17)

The coaxial detector geometry can be seen by the center dip in each graph. For each color-coded crystal a “center of gravity” of the response function can be calculated. It gives the position (angle) of each detector, which can vary slightly with the $\gamma$ energy. The precise position is useful for the determination

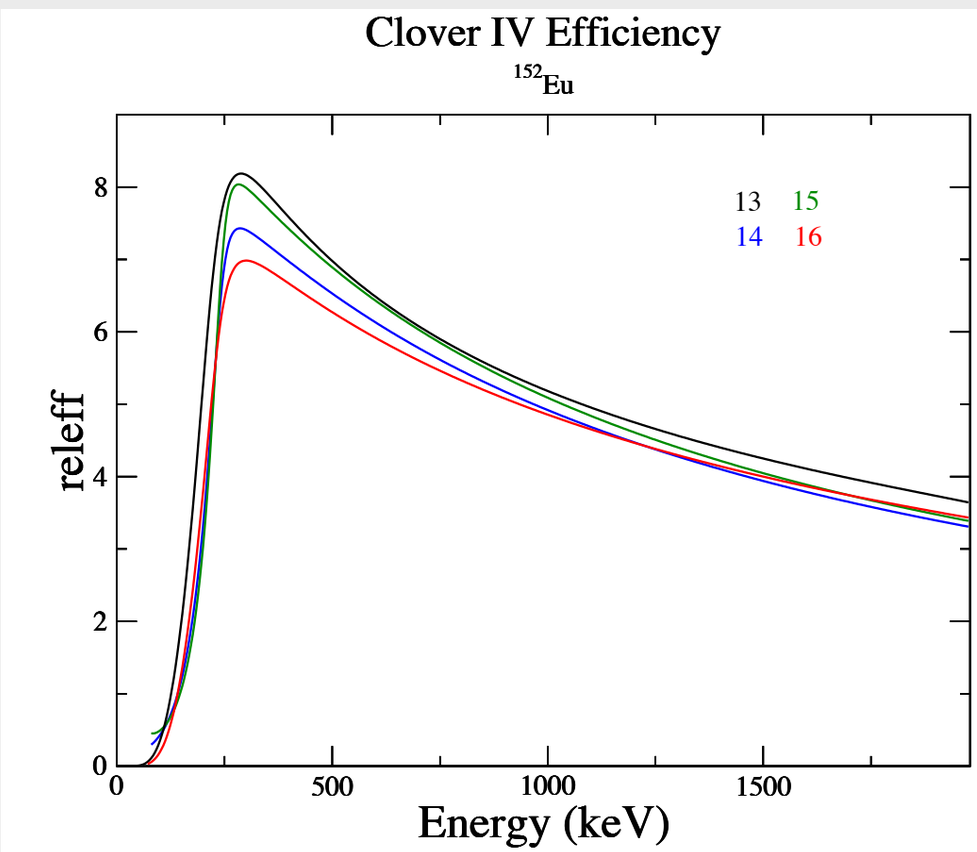


FIGURE 1.18 Relative efficiency curves of crystals in a clover

of the angular correlation. Equally important is knowledge of the relative detection efficiencies (Figure 1.18). These efficiencies are measured with a radioactive source at the target position, taken as singles. When coincidence conditions in the data analysis are applied these efficiencies can be different, because of certain cuts. When, as in rare cases, an isotropic γ transition exists in the spectra it can be used to check the ‘online’ efficiencies.

SECTION 4

# Angular Correlation

## Particle-$\gamma$ angular correlation

The spins of the excited nuclei are aligned perpendicularly to the beam direction. That is a direct consequence of the vector product of the beam velocity vector and the target nuclear spin, which is zero. In other words, with the beam direction as the quantization axis only transitions with the quantum number m = 0 are populated. This would be the ideal case for head on collisions. By selecting the recoil particles of the reaction in a particle detector with a finite opening, in reality, the alignment is not perfect. Therefore some m = ±1 substates are also excited. In addition, the $\gamma$ detectors have their own opening angle which smoothes the measured angular correlation further.

The angular correlation is written as

$$W(\theta) = 1 + \sum_{k=2,4,..}^{k_{max}} A_k \cdot Q_2 \cdot P_k(cos\theta) \qquad (1.2)$$

Here the $P_k$ (cos θ ) are the Legendre polynomials. Only even k's have to be considered, because of parity conservation in the decay, and $k_{max}$ is determined by the spins of the states and the multipolarity of the transition. The $A_k$ are the angular-correlation coefficients, which depend on the multipolarity of the γ-ray transition, and the $Q_k$ are the geo-

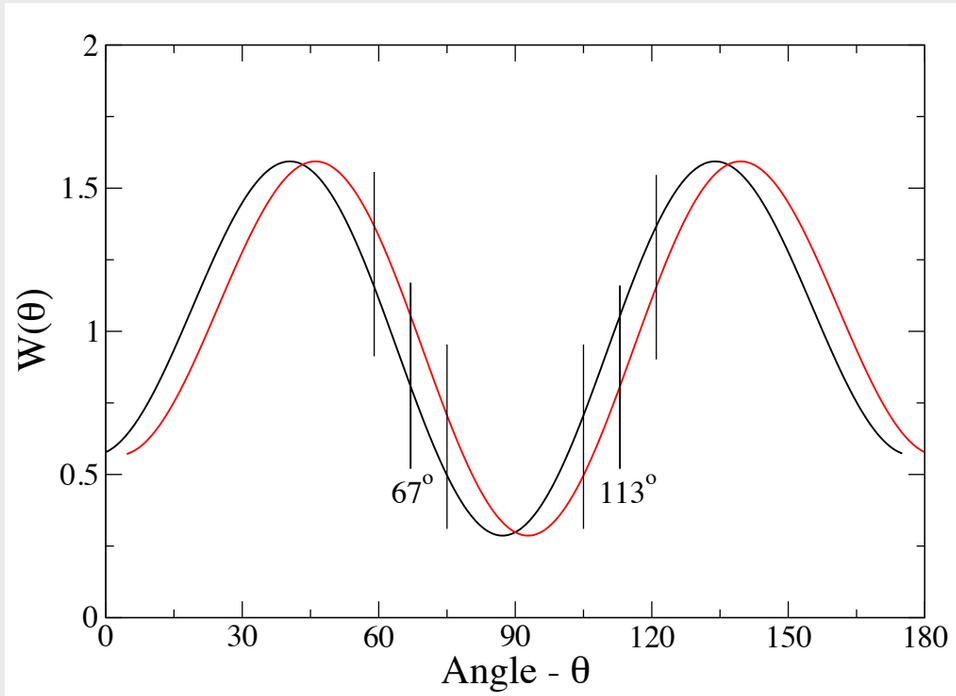


FIGURE 1.19 Angular correlation function for a 2→0 transition

The separation of the curves shows a shift of ±5 mrad. 67° and 113° are usual detector positions. The clover segments at the closest distance to the target are ±8° from the center as indicated by the vertical lines.

metrical attenuation coefficients accounting for the finite solid angle of the γ detectors. This formula describes the correlation in the rest frame of the decaying nuclei. If the nuclei decay at "high" velocity (e.g. v > 5%c) then relativistic corrections (Lorentz boost) have to be applied to the angle θ of the detector and to its solid opening angle.

## Correlation coefficients

The angular correlation can be determined in several ways.

For a Coulomb excitation experiment it could be calculated using a COULEX code which goes back to the early beginnings by A. Winther and J. de Boer (1965) [WI66].

But nothing beats the measurement of the correlation for a given experiment.

### 1. Direct Measurement

In a typical setup the γ detectors are mounted on a table and can be moved around the target chamber. Measurements are performed for a set of angles. This method takes extra running time, which may not be available.

The normalization of the measurements has to be done carefully, by using a monitor detector at a fixed angle or by knowing the integrated beam current for each run. Both methods have proven to be error prone. Often the range of angles that one detector can go to is limited when all the detectors are mounted.

The correlation coefficients are obtained from a fit to the measured data using equation (1.2).

### 2. Anisotropy ratio

When the angular correlation is known at two angles then the anisotropy ratio can be used to calculate the correlation coefficients.

Such a ratio can be obtained in various ways.

1. In the same way as in the direct measurement. Only two measurements are needed. One detector is moved to two positions. A properly normalized anisotropy ratio is calculated.
2. The following procedure is preferable because normalization problems are eliminated. A minimum of two detectors is used in each of two measurements. Each detector is set

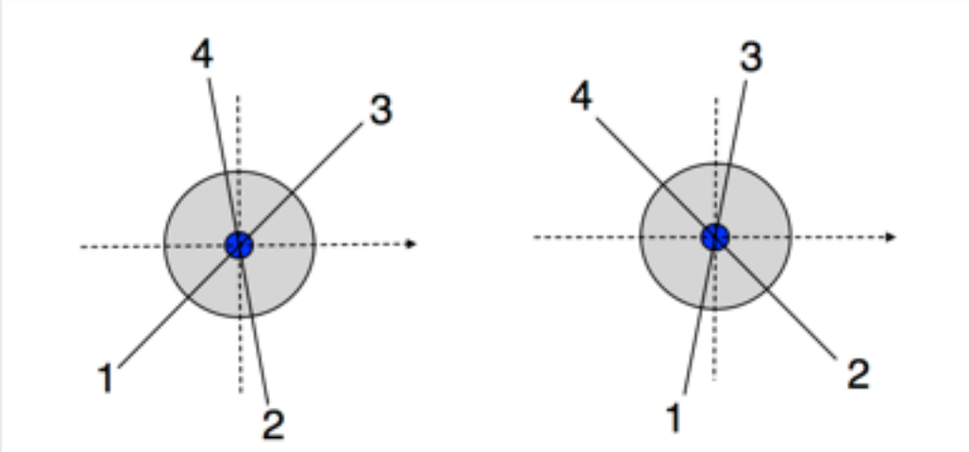


FIGURE 1.20 Detector placement for anisotropy ratio measurement.

successively to the same two the angles. The configurations for the two runs are shown in Fig.1.20. In praxis, in the first measurement  detector 1 is set at 135° (backward angle), and detector 4 is set close to 90°. To avoid absorption by the target frame an angle of 100° is preferred . In the second measurement the angles are interchanged. To double the statistics the other 2 detectors are employed simultaneously. The data of the two measurements are combined so that relative efficiencies and measuring times cancel in the ratio:

$$R_{i/j} = \sqrt{(N_i(\theta_1) \cdot N_j(-\theta_1))/(N_i(\theta_2) \cdot N_j(-\theta_2))}$$

$R_{1/4}$ and $R_{3/2}$ are independent ratios. For a 2→0 transition and angles of 50/80° one expects a ratio of about 2.0 for the full  clover, while $R_{1/3}$ and $R_{2/4}$ should be always 1.0 (cross check of the setup).

3. An anisotropy ratio can be obtained from the granularity of the clovers. The precession data for both up and down field directions are added and are corrected for relative efficiency differences. The angle separation between the clover crystals is taken from the detector scans.
4. In some experiments the detectors were moved periodically by a few degrees (± 2°) from the precession angle. The anisotropy ratio can then be derived in the same way as the precession ratio.

For a given anisotropy ratio the angular correlation coefficients can be calculated from Equation 1.2 using the so called η approximation:

$$A_k^{exp} = (1 - k \cdot (k+1) \cdot \eta) \cdot A_k^{theo}$$

As long as η << 1, the reductions of the angular correlation to due to the reaction and opening angles of particle and γ detectors  are well accounted for.

## 3. Using large detector arrays

Keep in mind, that the reaction plane is perpendicular to the magnetic field direction. Detectors in that plane are most sensitive to the rotation of the angular correlation. For an out-of-plane detector at an angle Φ, cos(θ) in the Legendre polynomials is reduced by a factor of cos(ϕ).

The relative efficiencies of the various detectors have to be known. Only detectors with the same opening angle can be combined. The relative efficiencies change with different  coincidence requirements and are usually not reliably known.

## Slope

Also called the logarithmic slope,

$$S(\theta) = \frac{1}{W(\theta)} \cdot \frac{dW(\theta)}{d\theta},$$

is needed to calculate the actual precession angle Δθ from the counting-rate change observed in the γ detectors as is discussed in the next section. It is useful to remember: The larger the slope the higher the sensitivity of the precession measurement.

## Attenuations

The actual measured angular correlation depends on the geometry of the γ and particle detectors.

For cylindrical γ detectors computer code exists to calculate the *Q's* in equation 1.2. A single clover crystal with a radius of 25 mm, a length of 80 mm, and an inner core diameter of 10 mm at a distance from the target of 130 mm has $Q_2 = 0.978$ and a $Q_4 = 0.928$. For a full clover (all four crystals) assuming some kind of spherical symmetry like a radius of 50 mm, length 80 mm, and an inner core 15 mm at a distance of 130 mm yields $Q_2 \sim 0.92$ and a $Q_4 \sim 0.75$.

This attenuation by the γ detectors has to be factored in when the angular correlation is calculated with the COULEX code. The COULEX calculation takes into account the opening angle and geometry of the particle detector and it is interesting to see how the particle detection defines the alignment, in other words the slope.

It was pointed out early on that a vertical slit in front of the particle detector "improves" the observed alignment [HOR75]. In Fig. 1.21 the slopes are calculated for a typical experiment: $^{106}$Pd on $^{12}$C at 280 MeV. The two angles, 59° and 75°, are positions of clover segments. For a circular particle detector (red and black curves) the slope decreases with the opening angle of the detector. The radius of the detector was varied from 3, 5, 7, to 9 mm. The situation is quite different for a rectangular particle detector. Although the value of the slope depends on

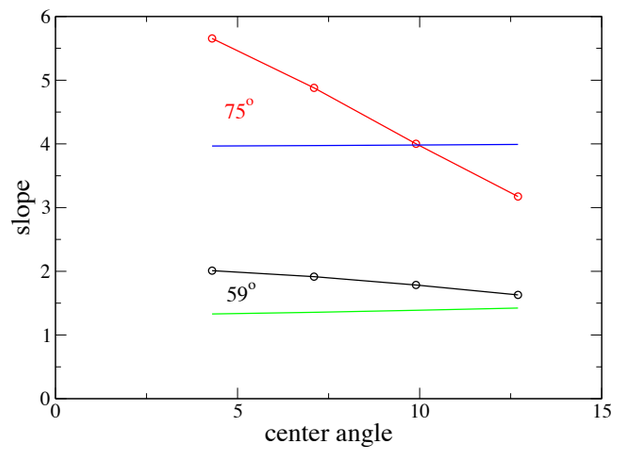


FIGURE 1.21 Calculated slopes for round and rectangular particle detectors.

The center angle is the angle in the middle of the detector. The red and black data points were calculated for a circular opening of the detector.

the width of the detector, here 9 mm, it barely changes with the vertical opening angle (blue and green curves).

## Recoil into Vacuum (RIV)

When highly ionized ions exit from the target foil into vacuum, hyperfine interactions occur while the electronic shell is restored, which cause the nuclear spins to precess. Since these hyperfine fields are randomly oriented, the rotations of the angular correlation yield an attenuation of the correlation.

In transient field experiments any attenuation is unwanted since it reduces the sensitivity of the measurement and there-

for a recoil out of the target or a detachment of the target layers should be avoided.

The size of the attenuation depends on the hyperfine field strength (Z and ion velocity), the *g* factor and the life time of the involved nuclear states.

RIV was early on recognized as an option to measure *g* factors [GOL82]. For readers interested, a paper by Randolph et al. [RAN73] applying RIV in a time differential measurement is highly recommended.

When the potential of transient fields was realized the method was basically forgotten. Especially the inability to determine the sign of the *g* factor was seen as a limitation.

The RIV method has experienced a revival in applications with rare isotope beams and the availability of multi-detector systems. Calibration of the hyperfine fields is still a problem. The attenuation is proportional to gτ. The life time τ of the state has to be known well and should be less than 3 ps. Readers are referred to recent publications [STO05][STU07].

The RIV as method to measure *g* factors is not part of this text.

Slowing down in a solid, even at high velocities, does not induce an attenuation of the angular correlation. The collisions are so frequent and the times between interaction are short, the spins are kicked back and forth, they basically stay in place until the electronic shells are completely restored. A measurement on a solid backed target where the ions stop essentially gives the unperturbed angular correlation.

# Precession measurement

Figure 1.22 shows again the detector positions and the reaction plane perpendicular to the magnetizing field direction. The beam projectiles impinge on the multilayer target. We are only interested in reactions occurring in the first layer of the target. The projectiles  which are Coulomb scattered, only about one in hundred will be excited, are stopped in the backing layer of the target. The lighter target nuclei of the reaction have sufficient energy to reach the particle detector.

## Particle-$\gamma$ coincidence

The coincidence of the light target ion and a γ-photon links the interesting events. Traditionally the simultaneity of the two is established electronically. Detector signals are recorded only when they occurred within about 500 ns to each other. This required many electronic modules, like timing filter amplifiers, discriminators, coincidence units, time-to-analog converters for the time branch and corresponding units for the energy. With an increase in the number of detectors, like 16 γ detectors, it is an unwieldy mess of modules and cables including the data acquisition system.

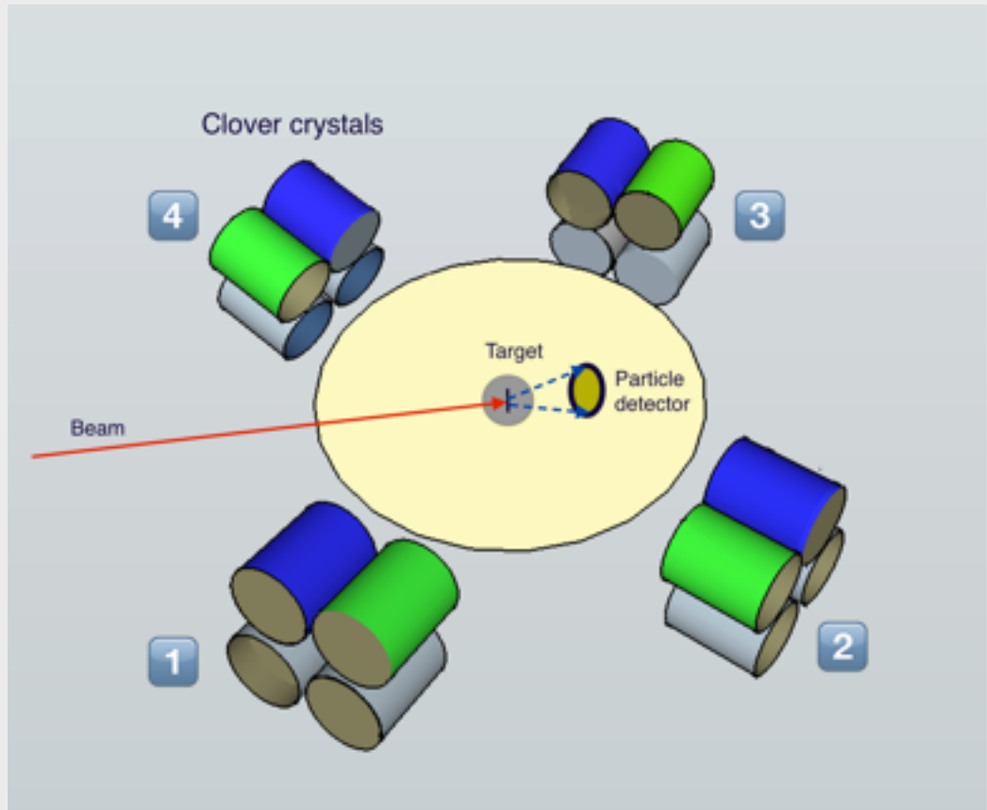


FIGURE 1.22 Detector layout for particle - gamma coincidence using four clover detectors and a downstream particle detector.

As an alternative, we use a commercial fully-digitized pulse processing system. Preamplifier signals of each detector are digitized with a 14 bit ADC at a 75 MHz rate in a PIXIE-4 system, time stamped and their pulse height determined. For each such singles event the information is stored in memory, buffered and written out to disk. Rates of up to 100 Mbytes/s can be written out.

The whole system (Figure 1.23) is compact and ideal for travel physics.

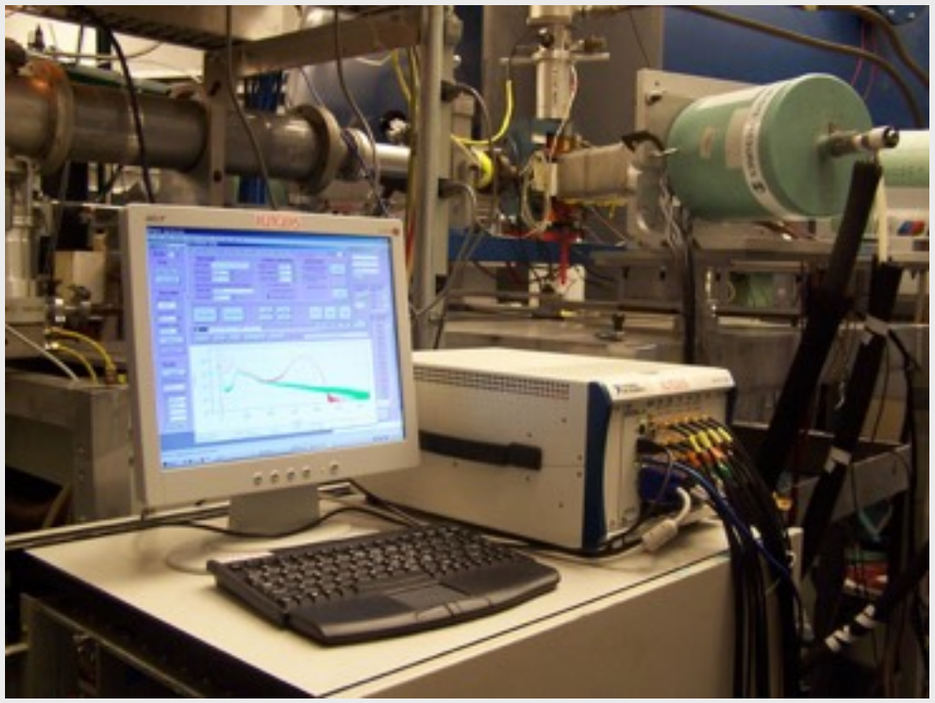

FIGURE 1.23 20 Channel Pixie-4 system from XIA in a National Instruments PXI crate.

Coincidence events are picked out by software. In a first step only particles and γ's with a time difference of less than 2 μs are selected. At the same time Compton add back is performed. The 4 crystals of a clover are connected to one four-channel digitizing module. When more than one channel in a module registered a γ at the *same* time, the gain matched energies were summed and added to the crystal with the highest γ energy. All γ spectra are gain matched on an event by event basis.

An event file is created using a simple list format: event header word including magnetic field direction and particle detector number, γ-detector number, particle energy, γ energy, and time difference between particle and γ. Such an event file contains a header block with all relevant information for sorting. In general, it should have all necessary information about the experiment, which is very useful when revisiting the data even years later.

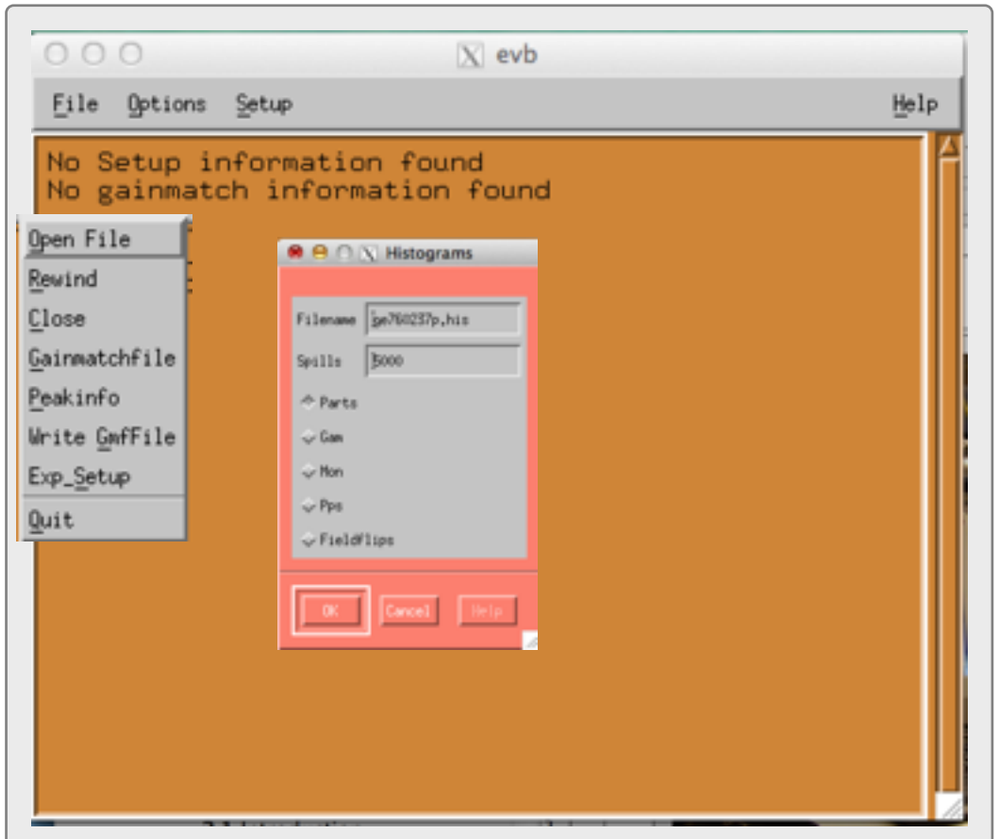


FIGURE 1.24 Event-builder program user interface

A suite of programs was written, for diagnosis and testing of the raw data. The main application is the event builder.

This application produces from the raw data, besides the event file, histogram files of particle singles, gamma singles, particles per second and field-flip files.

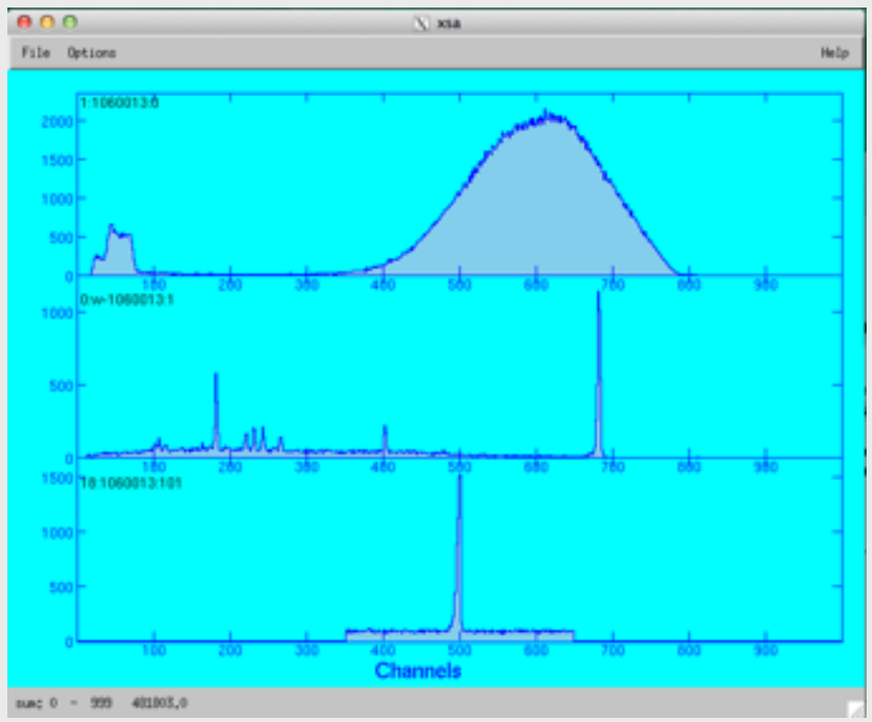


FIGURE 1.25 Unsorted event file data: $^{106}$Pd on C

Beam energy was 230 MeV. From top: particle, gamma and time difference spectra.

From such a list mode file histograms for each parameter are shown in Figure 1.25.

A data set, in this case, contains 33 spectra: 1 particle spectrum, 16 gamma spectra and 16 time-difference spectra. A time channel is 13.333 ns, limited by the digitizer frequency of 75 MHz.

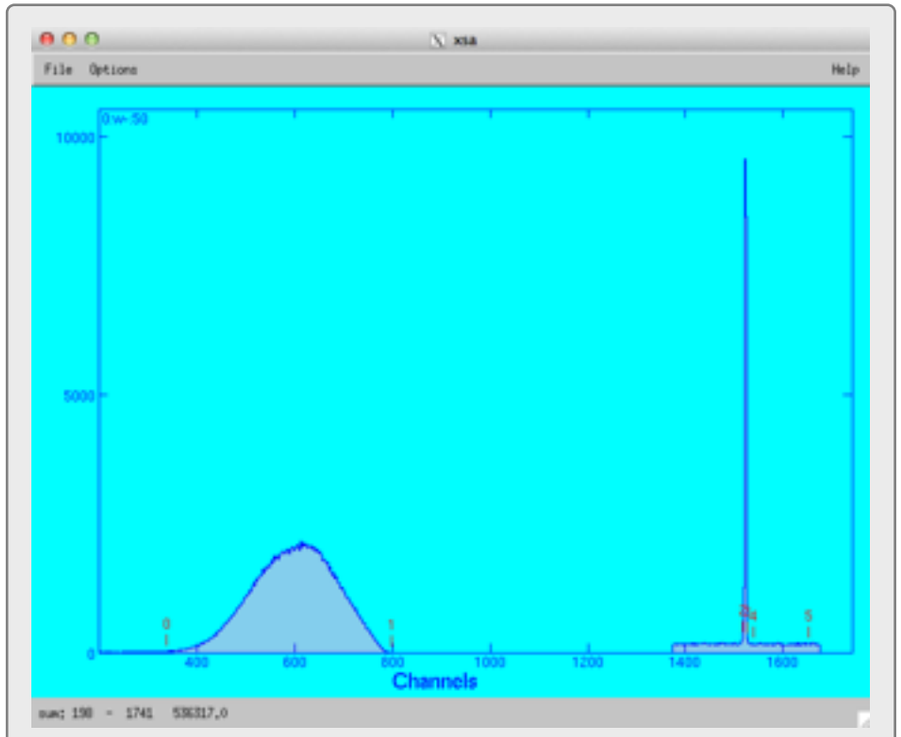


FIGURE 1.26 Particle energy and time cuts

The time cuts are a narrow cut around the sharp time peak and a wide cut for randoms selection. For the subtraction of randoms the corresponding spectra will be scaled according to their window width. The wider randoms window is chosen to reduce their error contribution to the prompt counts.

The event files are then sorted by setting constraints, cuts, on two event list parameters to produce spectra of the third, either time and particle energy to produce γ spectra (prompt and randoms), cuts on time and γ energies to produce spectra for corresponding particles or cuts on particle and γ energies to produce gated time spectra.

For the precession analysis gamma spectra are generated by selecting particle energy and time (Figure 1.26).

Applying these cuts and separating the data for each field direction results in a new data set of 64 gamma spectra, 4 spectra for each of the 16 clover crystals: prompt+randoms field up, prompt+randoms field down, randoms up, and randoms down.

## Up/Down analysis

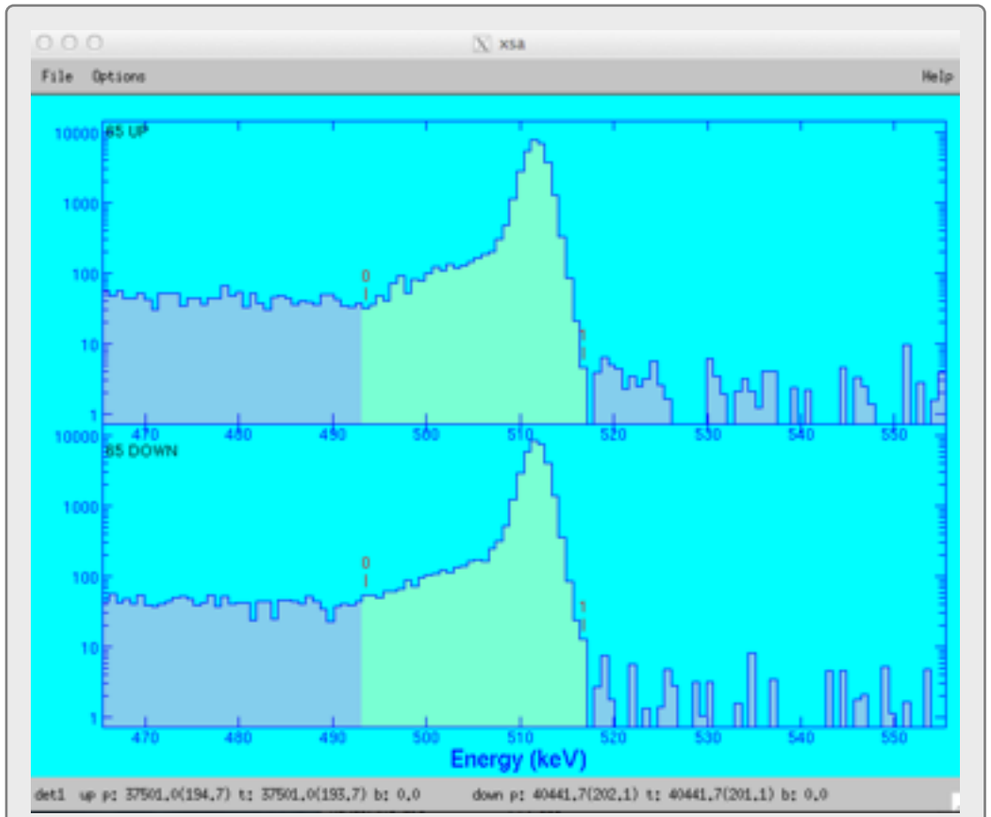


FIGURE 1.27 First $2^+$ in $^{106}$Pd. Up and Down spectra in Clover I

In this case no background had to be subtracted. There are basically no counts above the peak.

The up/down data set can be analyzed either for separate detectors, half clovers (combined data for crystals with the same angle θ) or full clovers. The analysis procedures are incorporated in the spectrum analysis program xsa.

The output for the 4 clovers:

```
UP   pos: 511.03    sum: 37501.0(194.7)  randoms: 2255.0
DOWN pos: 511.04    sum: 40441.7(202.1)  randoms: 2281.3
UP   pos: 512.11    sum: 53293.1(231.8)  randoms: 2452.9
DOWN pos: 512.14    sum: 49476.2(223.4)  randoms: 2406.8
UP   pos: 512.05    sum: 37560.6(194.8)  randoms: 2067.5
DOWN pos: 512.06    sum: 40872.0(203.1)  randoms: 2051.0
UP   pos: 510.99    sum: 43572.2(209.7)  randoms: 2211.8
DOWN pos: 511.01    sum: 40289.8(201.7)  randoms: 2218.2
```

The peak intensity for the transition of interest has to be determined from each spectrum. This includes proper background and randoms subtractions and statistical error calculations. A simple sum of the counts in a peak is usually sufficient, although in special cases, e.g. low statistics and/or symmetric peaks, a Gaussian may be fitted to the peak. The background is determined from a polynomial fit of various degrees to the

Individual ratios

```
eps(1) = -0.037729(0.003584)
eps(2) =  0.037140(0.003122)
eps(3) = -0.042220(0.003574)
eps(4) =  0.039141(0.003456)
```

data in regions left and right of the peak. In the example of Figure 1.27 no background was subtracted.

The difference in the counts for the two field directions ↑(up) and ↓(down) is due to the rotation of the angular correlation. If $N\gamma_1\uparrow$ and $N\gamma_1\downarrow$ denote the measured peak counts, ratios like

$$eps = \frac{N_{\gamma 1}^{\uparrow} - N_{\gamma 1}^{\downarrow}}{N_{\gamma 1}^{\uparrow} + N_{\gamma 1}^{\downarrow}}$$

give the individual rate changes in each detector:
More sophisticated double- and quadruple-ratios are constructed where the differences in relative efficiencies of the detectors and time differences for up and down cancel out. Double ratios for detector pairs like

$$\rho_{i,j} = \sqrt{(N_{\gamma i}^{\uparrow}/N_{\gamma i}^{\downarrow})/(N_{\gamma j}^{\uparrow}/N_{\gamma j}^{\downarrow})}$$

Double-ratio rate effect

```
File: 230ud  Peak: 511.01
                  up                        down
det        sum         sumerr        sum         sumerr
 1      37501.00      194.72      40441.69      202.14
 2      53293.09      231.82      49476.20      223.42
 3      37560.55      194.78      40871.96      203.10
 4      43572.17      209.71      40289.76      201.73

     ro 1,4   =  0.925975  +- 0.004634
     ro 2,3   =  1.082640  +- 0.005161
     ro 1,3   =  1.004508  +- 0.005110
     ro 2,4   =  0.997999  +- 0.004669

     RO TOTAL =  0.924821  +- 0.003196
     epsilon  = -0.039058  +- 0.001725
     epscheck =  0.001625  +- 0.001728
```

are constructed. With

$$\rho = \sqrt{\rho_{1,4}/\rho_{2,3}}$$

the rate effect is

$$\epsilon = (\rho - 1)/(\rho + 1)$$

Using the slope from the angular correlation the precession angle

$$\Delta\theta = \epsilon/S(\theta)$$

is obtained.

For this particular case of $^{106}$Pd the measured slope was S(67°) = 2.111(16) rad$^{-1}$ which is typical for this setup and beam energy. The experimental result for the precession angle is Δθ = -18.5 ± 0.8 mrad.

Remarks:

1. The life time of the 512 keV first excited state in $^{106}$Pd is 17.6 ps. Some nuclei decay in flight which contributes the ‘tail’ in the line shape of the peak (Figure 1.27).
2. The random counts in the peaks seem high, but one should remember that the beam projectiles can be Coulomb excited anywhere in the chamber and in the target.
3. epscheck is the double ratio rate effect for the detector pairings which show opposing rotations. Using $\rho_{1,3}$ and $\rho_{2,4}$ the effect should be zero, which it is within the given error. Deviations signal problems with the setup.

4. The sign of the precession depends on the magnetic field direction. The field direction depends on the current direction (poling of the power supply) through the coils of the magnet. All this has to be well established to obtain the correct sign of the magnetic moment.

5. The field direction is recorded with every particle. Reversing the polarity at the power supply can be done by a timer or particle preset. The interval (minutes) should be short compared to changes of the beam intensity and other long term variations in the experiment. The time it takes to reverse the field is short (the switching time of relays is in the ms range) and ignored.

6. The up/down analysis in xsa starts with the peak selection for each detector. An average of the up and down data is displayed. All selections are made in this window. The background regions are marked (the left side of peak has marks 0 and 1 - the right side 4 and 5 - both regions can be either on the left or right of the peak). Marks 2 and 3 select the peak region. The background fit parameters are determined from the averaged spectrum. The sum command then displays the up and down spectra (Figure 1.27) separately with the pre selected regions and with individually-calculated backgrounds. Only the constant term, the overall height of the background, is newly fitted for each spectrum. Nevertheless, it is important to judge the background carefully. In critical cases the background subtraction can strongly affect the precession effect.

7. For the up/down analysis ‘mistakes’ for instance, in peak region selection, if being applied consistently to both, up and down spectra, ‘cancel’ out in the double ratios.

## Calculation of the g factor

The measured Δθ is related to the g factor by

$$g = -\frac{\Delta\theta^{\text{exp}}}{\frac{\mu_N}{\hbar}\int_{\text{in}}^{\text{out}} B_{TF}(v(t), Z)\cdot e^{-t/\tau}dt}$$

- $B_{TF}(v(t), Z)$ is the velocity dependent transient field. It is calculated using the parametrization by numerically integrating the velocity dependence over the transit time through the ferromagnetic foil.

- $e^{-t/\tau}$ accounts for the nuclei decaying before leaving the ferromagnetic foil.

If g is known and Δθ is measured this relation can be used to calculate an average $B_{TF}$. The transit time, $T_{\text{transit}}$, can be calculated from the reaction kinematics. It should include $e^{-t/\tau}$.

### Sample input for transit calculation for $^{106}$Pd

```
|   1.   |   2.   |   3.   |   4.   |   5.   |  6.  |  Layer number
    C        Gd       Ta       Cu       Cu       Cu       Element
  0.442    3.34     1.40     4.49     5.6      0.0      Thickness in
mg/cm**2

1       : Number of target layer  ( = where excitation takes place)
2       : Number of ferromagnetic layer
46      : Z of the  Projectile
106     : A of the  Projectile
12      : A of the target layer
230     : Beam energy [MeV]
P       : Excitation of the Projectile [P] or the Target [T]
T       : Particle being detected: either Projectile [P] or Targer [T]
0       : Theta min.
23      : Theta max.
511.85  : Level energy [keV]
17.6    : Meanlifetime [ps]
0.670   : B(E2)-UP [(eb)**2]
1       : g-Factor
0.1950  : TF-Parameter [Tesla]

0.002   : Dicke [mg/cm**2] eines Intervalls fuer die dE/dx-Berechnung

R       : [R]ingdetector oder [S]chlitzdetektor
```

### Sample output

```
Values averaged over the different ion scattering angles and
depths within the target layer where the excitations occur :
============================================================

Diff. excitation cross section                 :  701.40 mbarn/sr
Excitations/sec for 1pnA beam current          :    2327
Average velocity when entering the ferromagnet :    7.00 v0
Average energy when entering the ferromagnet   :  128.97 MeV
Average velocity when leaving the ferromagnet  :    4.90 v0
Average energy when leaving the ferromagnet    :   63.01 MeV
Mean velocity within the ferromagnet           :    5.89 v0
Mean velocity of deexciting probe nuclei       :    0.29 v0
Time when entering the ferromagnet             :    0.07 ps
Time when leaving the ferromagnet              :    0.39 ps
Effective time period when TF is acting        :  324.75 fs
Precession angle                               :   43.88 mrad

100.0 % of the probe ions stop within layer # 5 (Cu).
Mean range within this layer           :    0.31 mg/cm**2

All ions to be detected reach the detector.
Their mean energy is                   :   48.48 MeV

The beam is stopped in layer # 5 (Cu).
Range within this layer                :    2.23 mg/cm**2
```

$$B_{TF} = \frac{\Delta\theta}{\frac{\mu_N}{\hbar} \cdot g \cdot T_{\text{transit}}}$$

$$B\ [\text{Tesla}] = \frac{\Delta\theta\ [\text{mrad}]}{0.047894 \cdot g \cdot T\ [\text{ps}]}$$

Consider a Δθ = 30 mrad and the transit time of 0.5 ps. For g = 1 B will be 1253 Tesla. The Rutgers parametrization assumes 100% magnetization for iron at 0.1706 T. When data from different targets are compared the individual target magnetization has to be factored in since $\Delta\theta \sim M$.

In praxis the expected precession $\Delta\theta_{g=1}$ is calculated for a given experiment, that is target parameters and reaction kinematics. We have adopted a computer program developed by the Bonn group (unpublished). The first target layer is subdivided in 10 layers and the opening angle of the particle detector is split into 10 rings with equal areas. With the adjusted beam energy of each of the 10 target layers, the reaction kinematics and Coulomb cross section into each angle segment is calculated. For each of the 100 bins the velocity dependent transient field is calculated using the parametrization. The relevant quantities are then averaged by weighting each bin with its relative cross section.

Remarks to the printout on the page before:

1. Target layer 5 is an extra Cu foil (beam stop), detached from the target and  placed directly behind the target.

2. Theta min and Theta max define the opening angle of the particle detector.

3. The TF-Parameter is the off-line measured magnetization of the target.

4. The last input item selects a circular (R) or slit (rectangular) particle detector.

5. In this case the probe ions were stopped not in the target but rather in the stopper foil. This potentially reduces the angular correlation due to what is known as “recoil into vacuum (RIV)” attenuation. Since the exit velocity was very low, this effect is expected to be small. No significant reduction of the slope was observed. In general, the target should be designed to stop the probe ions.

6. The calculated ‘Precession angle’ is the expected $\Delta\theta_{g=1}$.

   The g factor is then simply $g = \frac{\Delta\theta_{\text{exp}}}{\Delta\theta_{g=1}}$.

Chapter 2

# Real Data

**Sections**

1. Coulomb Excitation
2. Alpha Transfer

SECTION 1

# Coulomb excitation

## Kinematics

### 1. What particle spectra tell.

First lets recall some useful facts about Coulomb excitation. Coulomb excitation describes reactions where scattering partner interact only by an exchange of a virtual photon. Both partners are charged and can interact without “touching”. Below the Coulomb barrier in the center-of-mass system

$$E_{\mathrm{CM}} = \frac{e^2}{4\pi\epsilon_0} \cdot \frac{Z_p Z_t}{r_C(A_p^{\frac{1}{3}} + A_t^{\frac{1}{3}})}$$

the energy of the projectile is too low to overcome the distance of closest approach where the impact parameter b is equal to, or smaller than, the sum of the charge radii $r_t = r_C\sqrt[3]{A_t}$ and $r_p = r_C\sqrt[3]{A_t}$ where $r_C = 1.2 \; - \; 1.6\, fm$ depending on the source quoted.

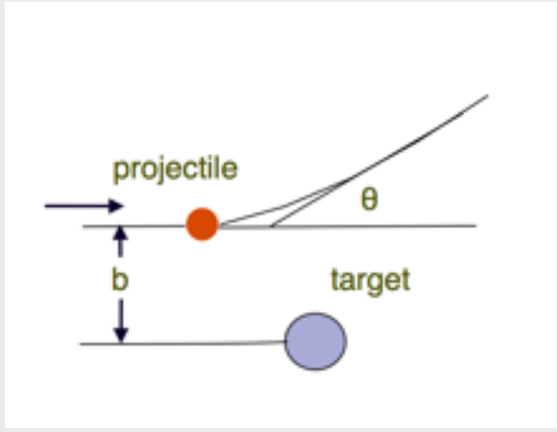


FIGURE 2.1 Schematics of scattering

For a projectile velocity the scattering angle θ depends on the impact parameter b.

In the lab system is $E_{\text{lab}} = \frac{A_p + A_t}{A_t} E_{\text{CM}}$.

The excitation cross section σ scales with B(E2↑) and increases with the projectile energy, but levels off above the Coulomb barrier.

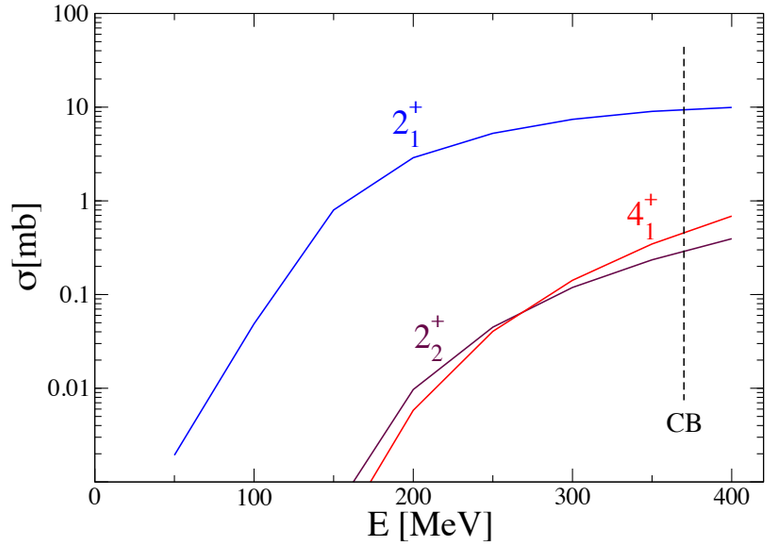


FIGURE 2.2 Coulex cross section for $^{106}$Pd on $^{12}$C

Calculated for the first excited states. CB indicates the Coulomb Barrier.

Coulomb excitation populates states from *below* and by choosing the beam energy the states of interest can be selectively excited. This is an important feature for TF measurements, since the nuclei precess in the state they are in, while traversing the ferromagnetic layer. If nuclear states are fed from *above* the lower states inherit the precession from the feeding states. Therefore the decay history of such excited nuclei has to be considered case by case.

## Kinematics

In inverse kinematics a heavy projectile impinges on a light nucleus. All scattering products move after a collision in the lab system forwards. In the center of mass system particles can also scatter backwards and two solutions exist. The heavy partners are confined in a cone with a small opening angle, determined by the mass ratio of the reaction partners:

$$\psi_{\text{max}} = sin^{-1}(A_P/A_T)$$

independent of their energy. In the case of $^{106}$Pd on $^{12}$C this angle is 6.5°. The corresponding carbon angle is 40°. For a typical particle detector opening angle of ±24° the projectiles scatter into a cone of a maximal angle of 5.2°.

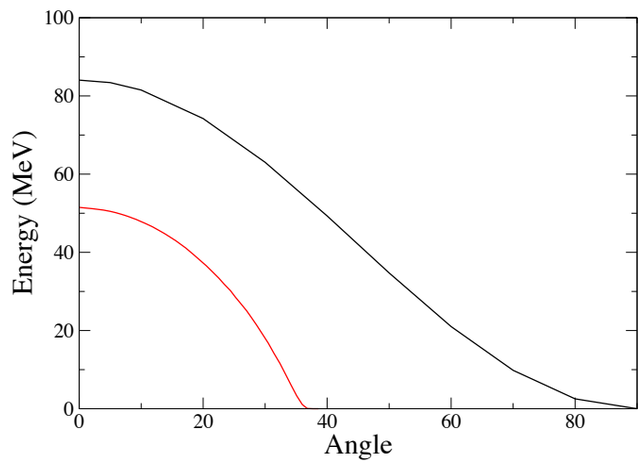


FIGURE 2.3 Energy of detected C versus scattering angle.

$^{106}$Pd scattered on C at 230 MeV. The red curve takes into account the absorption in the target and beam stopper foils

The carbon nuclei come with a broad energy distribution. Their energy is determined by the scattering angle (Fig,2.3).

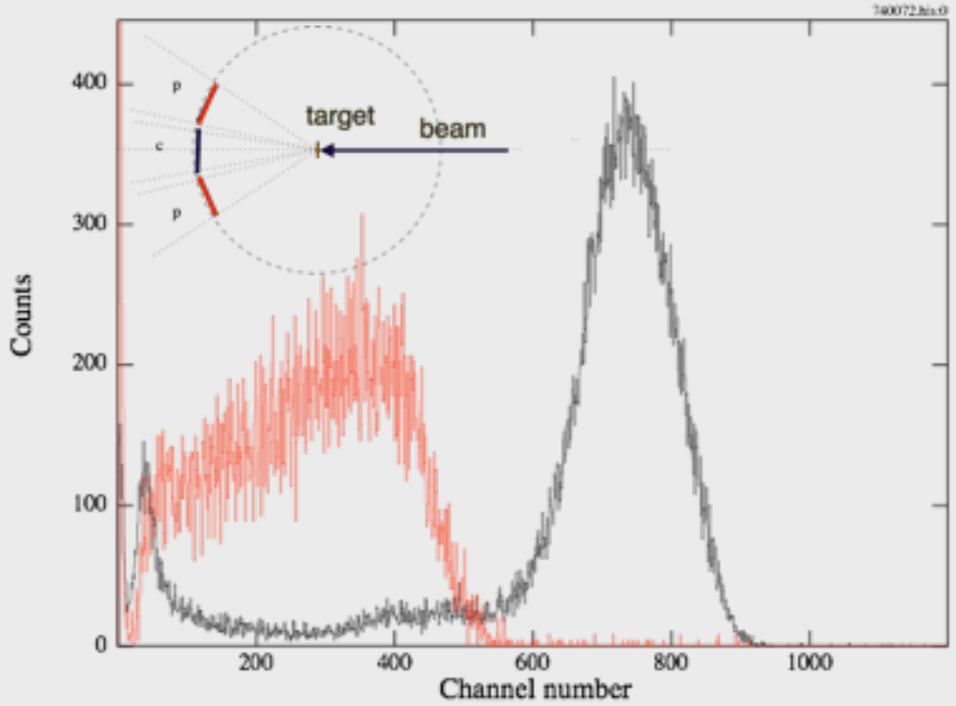


FIGURE 2.4 Split particle detector spectra.
Red outer (peripheral) solar cells, black center cell.

The above picture (Figure 2.4) shows particles taken with the triple solar-cell array (left side of Fig. 1.12).The black graph shows the particles recorded in the center detector, while the red histogram is the sum taken with the peripheral detectors (the same preamplifier was used in all detectors for this picture to preserve the energy scale). The particles scattered near zero degrees have the highest energy. At larger angles the particles have less and less energy and finally fall below the detection threshold. Two remarks: the slopes for the two particle groups in Figure 2.4 are very much the same (rectangular detectors) and the number of particles detected are similar for all cells. Hence it can be concluded that having a fancy detector array adds little to no extra information.

Let's explore particle spectra for different beam energies. Shown in Figure 2.5 is a sequence of spectra taken with a $^{56}$Fe beam. The Coulomb barrier for $^{56}$Fe on $^{12}$C in the lab system is about 132 MeV. The particle detector was a 300 mm²

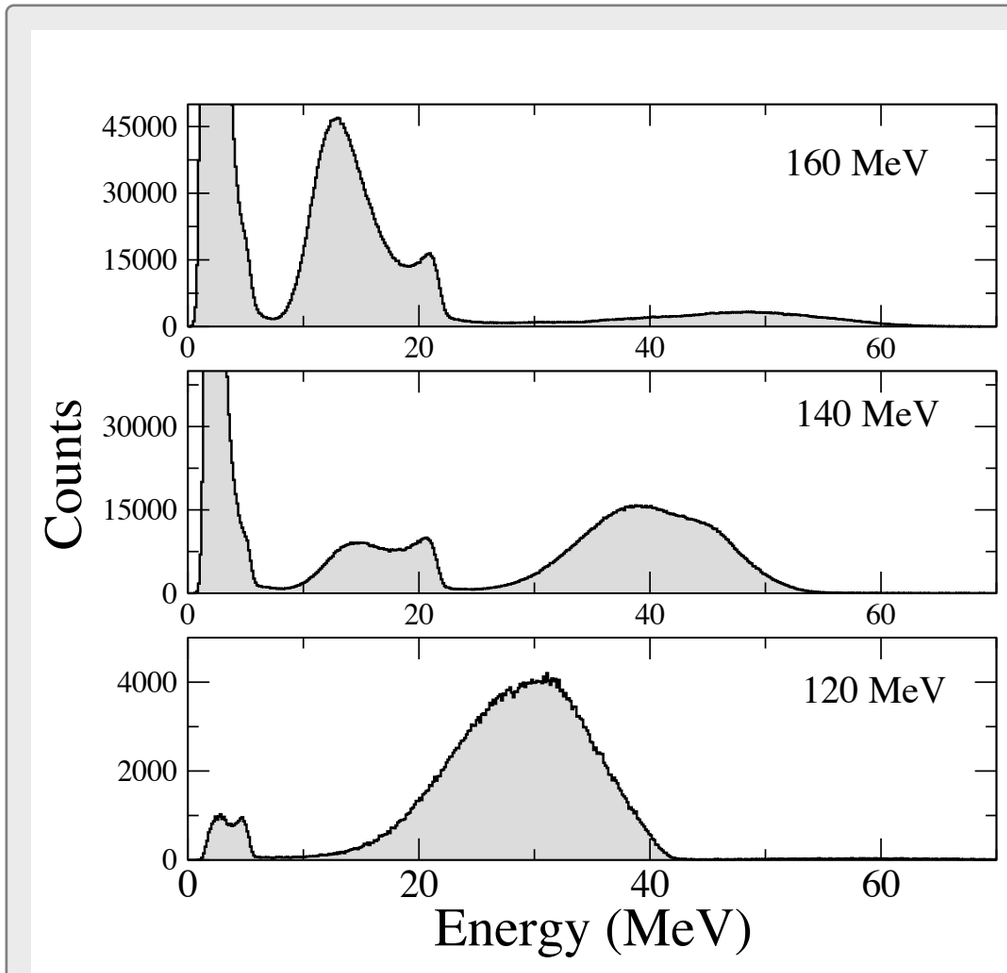


FIGURE 2.5 Coincident particle spectra: $^{56}$Fe on $^{12}$C below and above the Coulomb barrier.

PIPS placed 23 mm downstream of the target (opening angle ±23°).

At 120 MeV, well below the Coulomb barrier, only the carbon peak and some low energy particles are detected. Actually, these low-energy signals come from high-energy, light particles. These particles are not stopped in the detector but lose some of their energy. The detector records a ΔE signal. It was not clear where these particles come from, but they were beam-related and not detector noise. About 95% of the detected particles were carbon ions.

At 140 MeV, just around the CB, the beam energy at the exit from the carbon layer is 125 MeV, the spectrum has changed dramatically; the carbon is shifted to higher energy (because of the higher beam energy) and a middle structure plus a sharp low energy peak appeared. New reaction channels have opened. They produce lots of light particles which again are not stopped in the detector. Both low-energy-peak structures are ΔE signals.

At 160 MeV it can be seen, that the new reaction channels dominate and the Coulomb scattered carbon is only a small part of all particles. At 140 MeV about 35% of the particles are from Coulomb-scattering. At 160 MeV this number is down to less than 10%.

Although the Coulomb excitation cross section still rises above the CB and higher excited states are increasingly excited (Figure 2.2), the total reaction yield is so diminished that measurements become cumbersome. In addition, another disadvantage is a reduction of the observed spin alignment due to interference near and above the CB, which further reduces the sensitivity of the precession measurement. The Coulomb excitation has to be carefully evaluated if higher excited states, even $4_1^+$ states, are considered. Targets heavier than C targets are a good choice.

The different particle groups can be identified from the γ spectra. A good example is $^{46}$Ti at 100 MeV on a C target (CB =

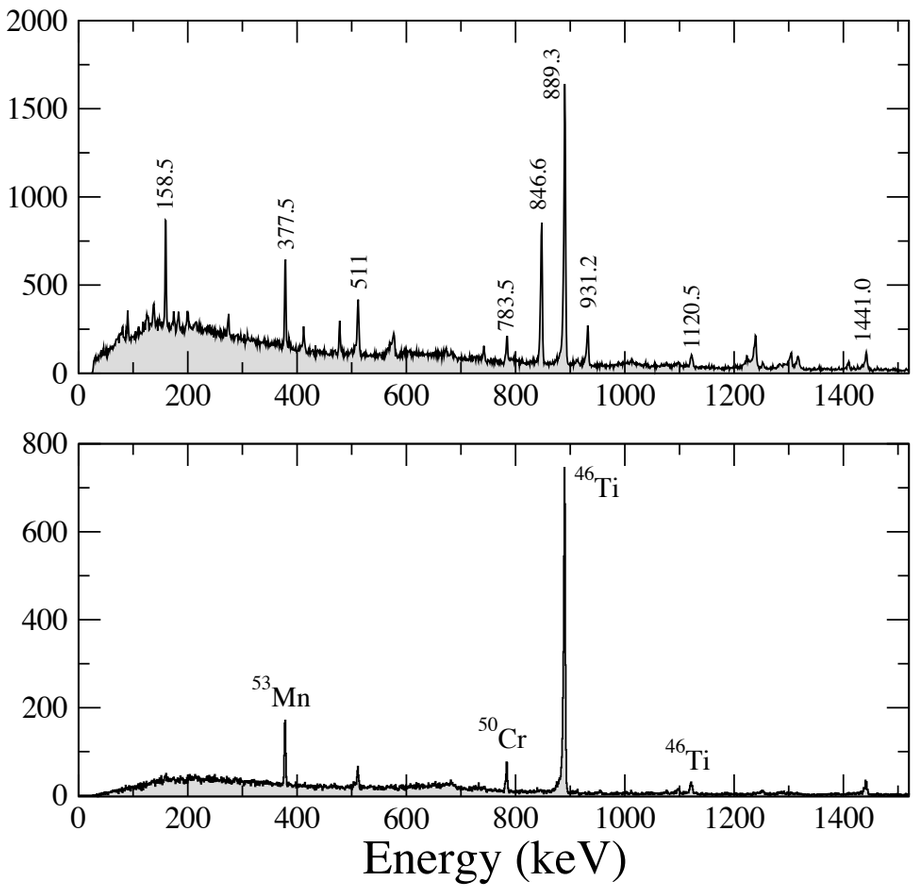


FIGURE 2.6 Coincidence γ spectra from $^{46}$Ti on $^{12}$C

At the bottom the low energy particles were cut. Low lying states in $^{50}$Cr and $^{53}$Mn were observed.

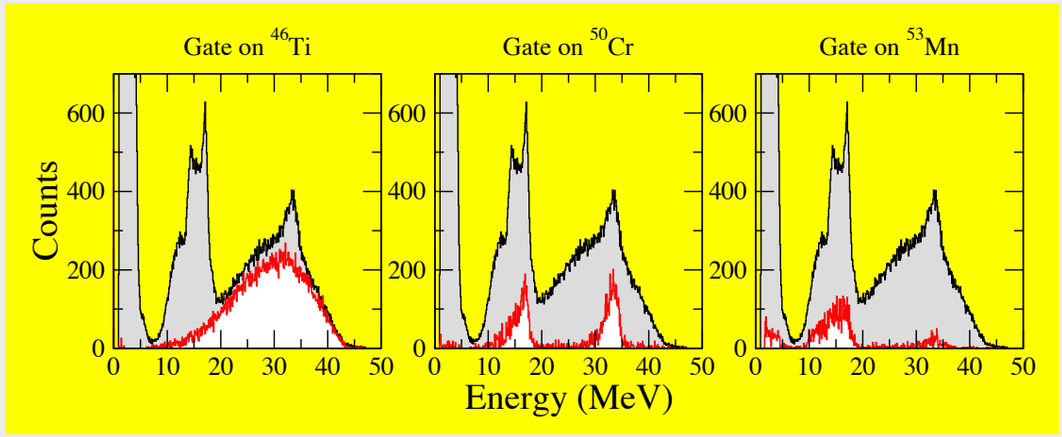


FIGURE 2.7 γ-gated particle spectra. All particles are shown for comparison.

100.7 MeV). In Figure 2.6 the top γ spectrum contains a number of lines, coincident with all particles in the event file. When only particles above 10 MeV were selected then the bottom spectrum shows besides $^{46}$Ti mainly transitions in $^{50}$Cr and $^{53}$Mn. Putting gates on these γ lines yields the spectra of Figure 2.7. From left to right, the first picture shows as an insert the particles associated with the Coulomb excitation of $^{46}$Ti. The insert in the middle picture shows two peaks, with the high energy peak having about twice the energy of the first peak. These particle groups are α particles. They are in coincidence with γ's from $^{50}$Cr. The $^{50}$Cr is created when $^{46}$Ti projectiles pick up an α particle from $^{12}$C. This α-transfer reaction is an important reaction channel and will be covered in detail in the next section. In the rightmost picture of Figure 2.7 the gate is set on γ's belonging to $^{53}$Mn, which is an incomplete fusion product of $^{46}$Ti and $^{12}$C, or a two alpha transfer plus the loss of one proton. The associated particles are mainly α particles.

The low-energy particle peak in Fig. 2.7 contains about 90% of all the particles, it goes up to 300000 counts on that scale. A γ spectrum in coincidence with these particles is shown below. Despite of the presence of so many particles, the associated γ spectrum is relatively clean (Figure 2.8).

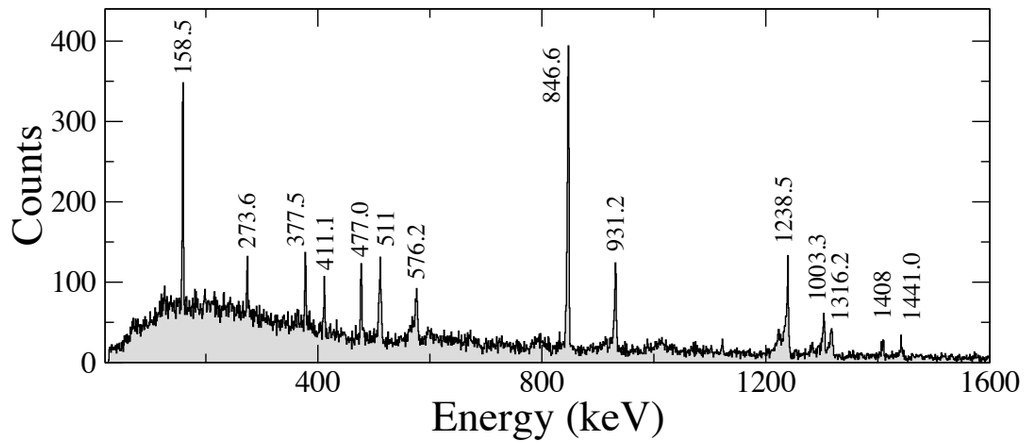


FIGURE 2.8 γ rays in coincidence with the low energy particle peak

# Alpha Transfer

Carbon may be the best example of an alpha-cluster nucleus.

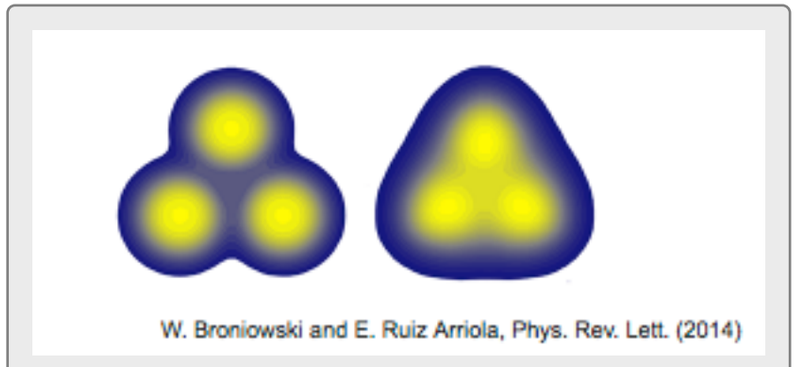


α-cluster model of the $^{12}C$ ground state

In inverse kinematics experiments on carbon at energies near the Coulomb barrier the pick-up of an α particle by the projectile is strongly observed. If the above picture applies then the radius of a carbon nucleus may not be well defined. As a matter of fact, the α-transfer reaction is already observed at beam energies below the traditional Coulomb barrier.

The projectile plus the α particle fuse into a new nucleus under conditions that are suitable for a transient-field experiment.

The α-transfer reaction is attractive for transient field measurements, because it opens the door to measuring unstable nuclei, which otherwise can only be produced as radioactive beams. Radioactive beams are not readily available and, when, they have very low intensities. As will be pointed out later, radioactive beams come with their own set of problems.

Below is an incomplete list of α-transfer reactions that have been used to measure g factors with the transient field method:

$^{40}Ca \rightarrow {}^{44}Ti$

$^{58}Ni \rightarrow {}^{62}Zn$

$^{64}Zn \rightarrow {}^{68}Ge$

$^{84}Sr \rightarrow {}^{88}Zr$

$^{78}Kr \rightarrow {}^{82}Sr$

$^{86}Kr \rightarrow {}^{90}Sr$

$^{96}Ru \rightarrow {}^{100}Pd$

$^{106}Cd \rightarrow {}^{110}Sn$

Nevertheless, from an experimental point of view, Coulomb excitation is by far the preferable reaction. Here is why:

- in an α-transfer reaction the spin alignment is small.
- the incorporation of the α particle into the projectile leads to higher internal excitation and therefore to the population of higher excited states. Feeding corrections in the decay have to be considered.

The α-transfer reaction from carbon is not well studied. Here are some observations which have emerged so far.

First take a look at the particle spectra again. The example $^{12}C(^{46}Ti,^{8}Be)^{50}Cr$, shown in Figure 2.7 center, has two peaks. The $^{8}$Be is unstable and breaks up immediately into two α particles. Both α particles have about the same energy. If both α particles reach the detector the higher signal is recorded. If only one of the two α particles hits the detector, only about half of the energy is deposited. This double-peak structure is characteristic for the α-transfer reaction. In the $^{46}$Ti example the α particles from the Be breakup have an energy of ~17 MeV each (after passing all of the target and foils), too much for stopping in 100 µm of Si. The observed peak energies therefore are not the full absorption peaks. This is important to know, since the peaks can be 'moved around' in the spectrum by varying the detector thickness (for example, by a change in bias voltage), by selecting the opening angle of the detector (distance to target) and by the placement of extra absorber foils. It helps to obtain well separated particle groups in the spectra so as to set gates on the α-particle peaks and produce clean, low-background γ spectra. Examples can be seen in the spectra of Figure 2.9. A beam of $^{88}$Sr was accelerated to energies close to the CB on carbon, which is ~270 MeV. The particle groups are well separated. At 260 MeV, just below the CB, the α transfer to $^{92}$Zr is already observed. At only 10 MeV more the increase of light particles can be

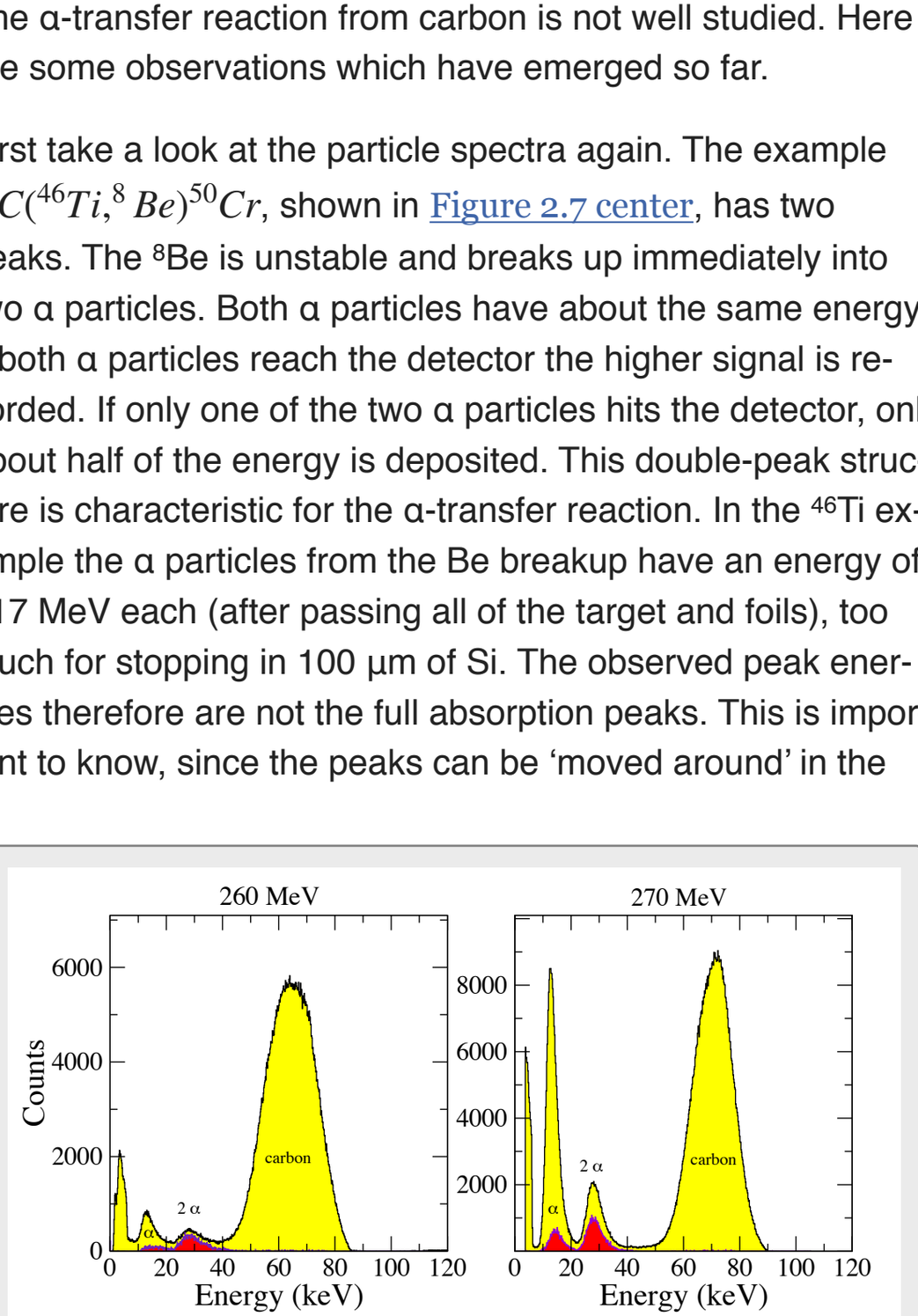


FIGURE 2.9 Particle spectra near the Coulomb barrier

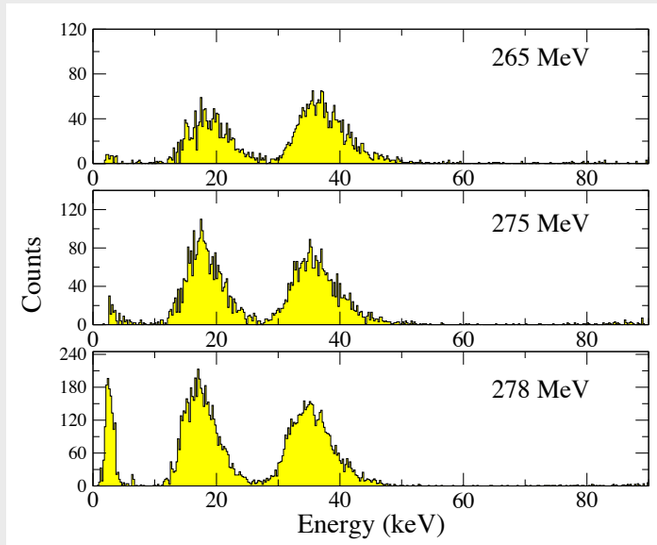


FIGURE 2.10 Alpha-particle spectra from $^{84}$Sr on C. The double peaks are two α's (right peak) and one α detected, respectively.

The intensity ratio of the two peaks changes with the beam energy. The Coulomb barrier for $^{84}$Sr on $^{12}$C is 261.5 MeV. The beam loses 30 MeV within the carbon.

seen. How much the α transfer actually increased is hard to quantify, because of a missing beam-current normalization.

Unfortunately, excitation functions for the α-transfer reaction were never measured. Nonetheless, below are some qualitative observations.

- The intensity ratio of the α-to-2α peaks increases with energy. A gate on the 1-α peak does not yield clean γ spectra, since other reaction channels cannot be excluded.
- The α-transfer reaction is a resonance like process and peaks near the CB. There are indications that at higher energies the α transfer decreases sharply and finally is not seen at all.

The optimal beam energy for the α-transfer reaction seems to be close to the CB. It should be kept in mind that in a typical transient-field experiment the carbon target layer is “thick” and the beam loses a fair amount of energy in the carbon layer. Some numbers: a 270 MeV beam of $^{88}$Sr loses 30 MeV in 0.6 mg/cm² of carbon.

It is desirable to carry out measurements on a thin carbon target (0.1 mg/cm² corresponds to 3 MeV at 100 MeV of Ti) with equally fine steps of the beam energy with excellent beam intensity normalization. At the same time the angular distribution of the α-particles should be measured.

CHAPTER 3

# Selected Experiments

**Sections**

1. **Strontium Isotopes**
2. **Radioactive Beam experiments**

In this chapter some published experiments will be discussed.

Nuclear chart

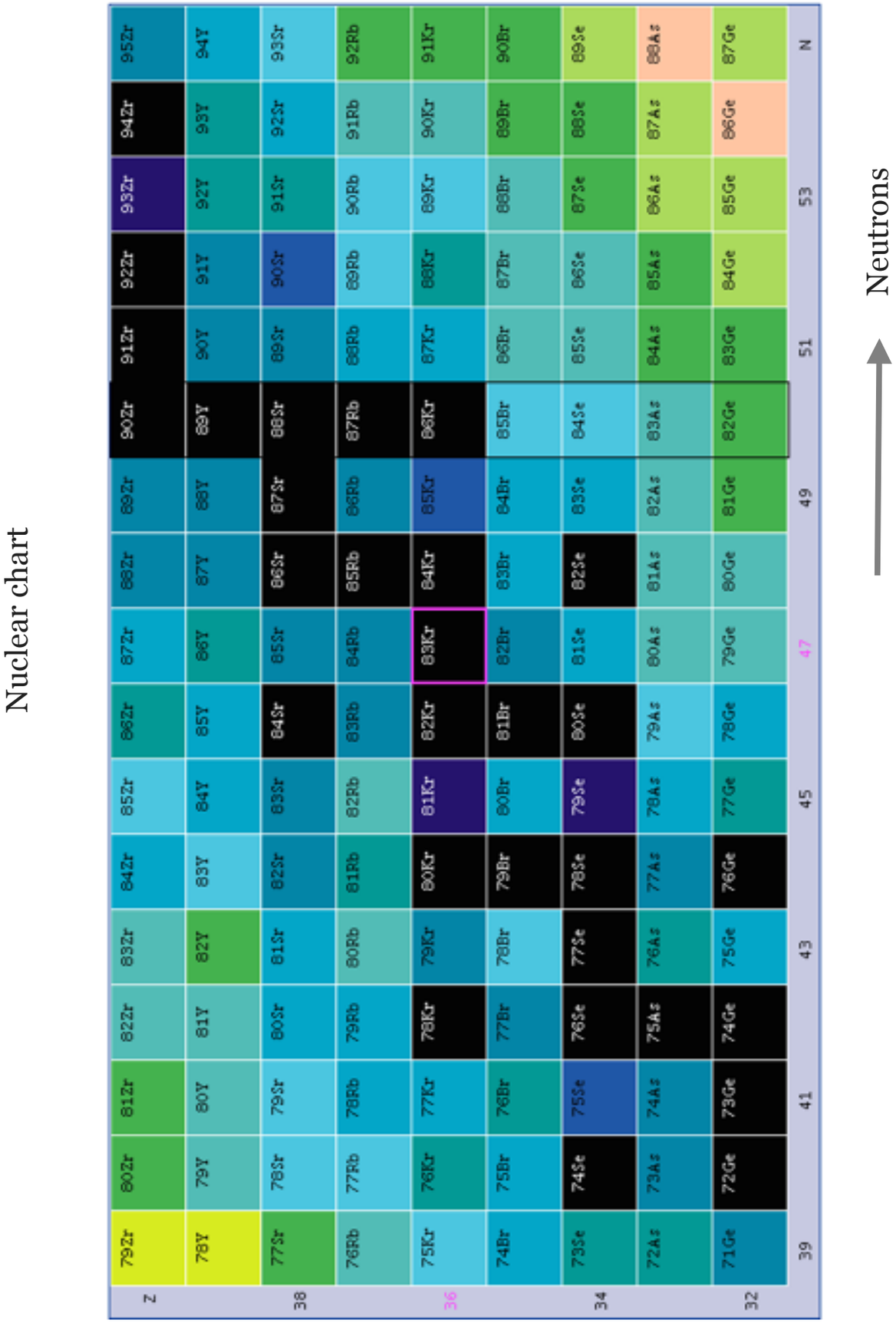

Applying mono-isotopic beams allowed magnetic-moment measurements across whole isotopic chains. Clean beams can be provided, even if the natural abundance of some of the isotopes is quite low. In a few cases small amounts of enriched materials were used to boost the output.

In such experiments, the *g* factors of all the available isotopes in a chain can be measured with one standard target. The measured precession angles are directly proportional to the *g* factors. Small adjustments to the beam energy help to keep the velocity range of the ions within the ferromagnetic layer for all the isotopes as equal as possible. Such sequences of relative *g* factors can be measured with high statistical precision. The relative *g* factors are independent of calibration issues and provide data which can be used to test theoretical ideas systematically by varying one parameter (here the neutron number) at a time.

Experimentally challenging, but very desirable, is the extension of the *g*-factor measurements beyond the stable isotopes. A world-wide effort is underway to provide radioactive nuclei as beams. The transient field technique in inverse kinematics has been tried with such beams. Few experiments have been published so far and some will be visited later.

There is a long list of *g*-factor measurements on stable isotopes, ranging from $32 < A < 140$. Most experiments were done with Tandem Van de Graaff accelerators. For the heavier elements at higher beam energies and for noble-gas beams (Ar, Kr and Xe) cyclotrons, but also heavy-ion linear accelerators, were used. A tandem accelerator is limited to elements for which negative ions can be made in the ion source. For the other accelerators a common ion source type is the Electron Cyclotron Resonance or ECR source which provides multiply-charged positive ions of any element.

The compilation of *g* factors in Figure 3.1 shows the sensitivity of the magnetic properties to the nuclear structure near the closed shell for N = 50.

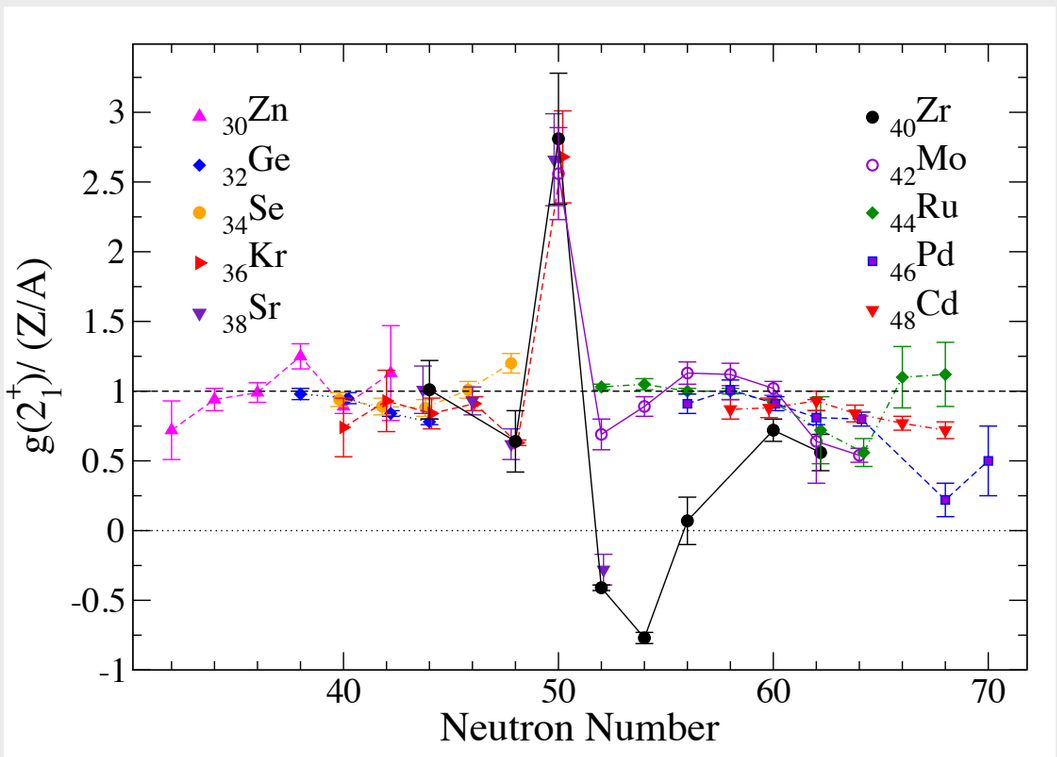


FIGURE 3.1 Compilation of g factors of the first excited state in even-even nuclei. The values are normalized to Z/A, the collective prediction with all the nucleons contributing.

As expected, near closed shells single-particle excitations dominate the nuclear structure. Thus, with the neutron shell

closed at N = 50, the proton excitations predominantly contribute to the first excited state. Indeed, all the measured g factors for N = 50 nuclei are positive and large. Away from closed shells, both protons and neutrons contribute and their contributions to the wave function are reflected in the *g*-factor value. In the middle between closed shells the *g* factor is often close to the collective value Z/A, basically reflecting the nucleus as a whole. In Figure 3.1, therefore, this contribution is factored out, with all the *g* factors being divided by Z/A. The deviations from **one** then clearly indicate the sensitivity of the results to the underlying nuclear structure details.

An interesting highlight of Figure 3.1 are the negative g factors. Negative g factors can only arise from dominant neutron contributions. This happens here only for Zr and the newly measured $^{90}$Sr. The reason has to do with the proton configuration in these nuclei. Zr has 40 protons. In the simplest picture the $2p_{1/2}$ proton orbit is fully occupied. Z = 40 is considered a closed subshell and the proton core is inert. The situation for Sr is less clear. Z = 38 also has a filled last proton orbit, $1f_{5/2}$. The negative *g* factor indicates that the protons mainly like to stay in the closed orbit. However, some proton contributions are needed in Zr and Sr to account for the lower than expected observed magnitude of the *g*-factor values.

# Strontium chain

The *g* factors of the $2_1^+$ states in the stable Sr isotopes were measured 1987 by Kucharska et.al. [KUC88] and also at the Yale tandem in 2012 [KUM121]. Lately, measurements on the Sr-isotope chain were extended on both sides of the line of stability to $^{82}$Sr and $^{90}$Sr by using the α-transfer reaction with beams of $^{78}$Kr and $^{86}$Kr [KUM14]. These measurements were also intended to shed light on the robustness of $^{90}$Zr and $^{88}$Sr as closed core nuclei in shell model calculations.

The measurements were done at the K500 super conducting cyclotron at Texas A&M University. This is a high energy machine and rarely used for heavier ion beams and relative low beam energy. Fine tuning of beam energy takes time. The first choice of beam energy was 3.2 MeV/u. The idea was to keep the beam energy of the $^{86}$Kr ions above the Coulomb barrier throughout the carbon target (the beam of 275 MeV loses 28 MeV in 600 µg of C, the Coulomb barrier is 252 MeV).

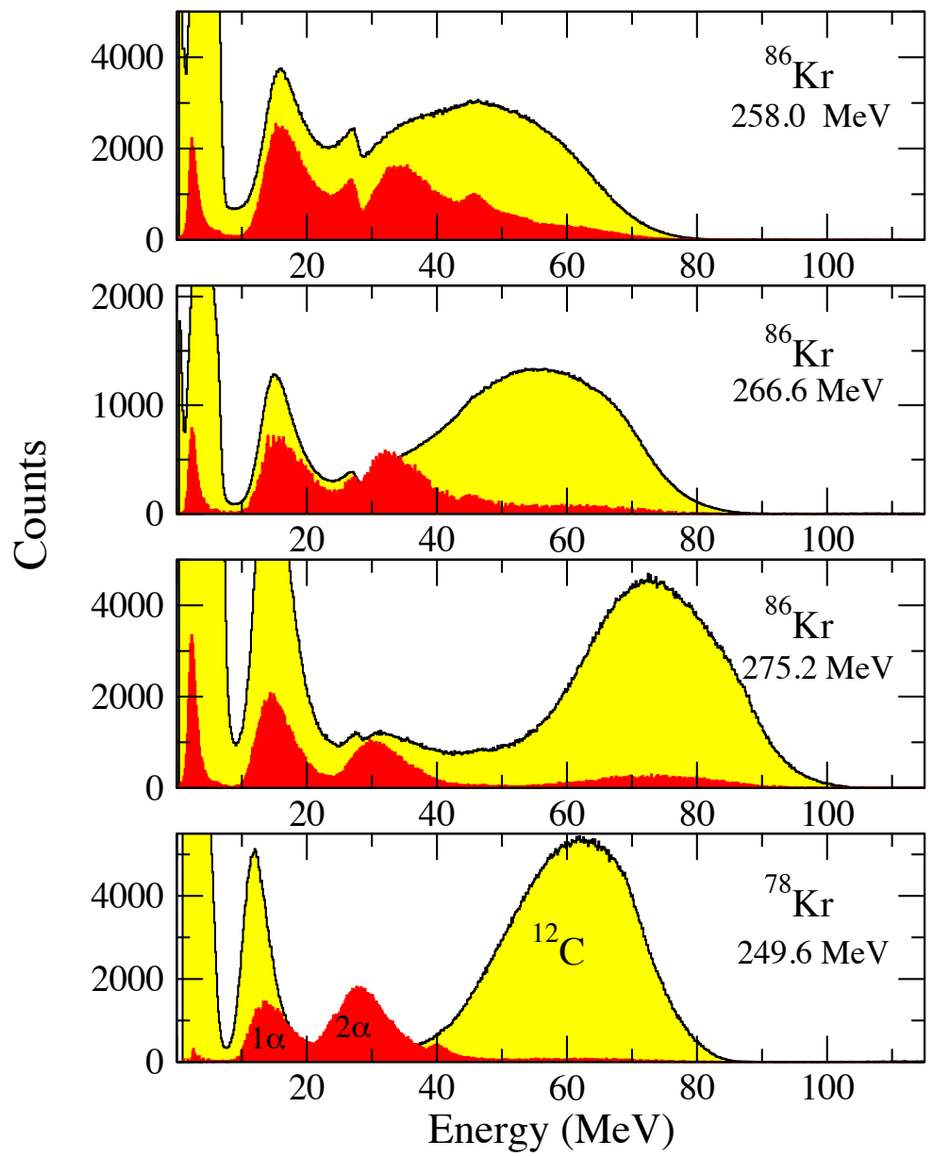


FIGURE 3.2 Particle spectra including α-transfer reaction.

Surprisingly, after the beam was switched to $^{78}$Kr, a much higher α-transfer yield was observed. This effect was attributed to a beam energy closer to the CB. The CB for $^{78}$Kr on

$^{12}C$ is at 235 MeV. The particle spectrum is shown as bottom spectrum in Figure 3.2.

Therefore, an effort was made to run $^{86}Kr$ beam at lower energies (see top spectra of Figure 3.2). The yield of the α-transfer reaction indeed increased, but the α-particle energy in the particle spectra was spread out. Setting particle gates to produce clean γ spectra was more difficult.

In these experiments the Coulomb excitation of the Kr beams measured simultaneously with the α-transfer reaction served as monitor for the experiment and Sr results. Having such a monitor is important when, as in this case, small results are obtained.

# Radioactive beam experiments

## $^{76}$Kr: First g-factor measurement using a radioactive beam

Radioactive $^{76}$Kr has a half life of 14.8 h. This makes it a good candidate for separating its production and its reuse as beam. In 2003, in several test experiments at the 88 Inch Cyclotron in Berkeley the reaction $^{74}$Se(α,2n)$^{76}$Kr was used to produce, extract and collect $^{76}$Kr as a gas [CBM04]. After bombarding the Se for about 17h, the highly activated target was heated in situ above the melting point of selenium in a He gas stream. The emanated Kr atoms were frozen out from the carrier gas in a LN cold trap. Warming the trap released the krypton gas into a holding reservoir, which provided a $^{76}$Kr beam for about 2 h. The beam intensity over the two hour period varied from $10^8$ to $10^7$ particles per second on the target for the experiment. This is a high intensity for radioactive beams. The production and separate acceleration guarantied a pure $^{76}$Kr beam on target.

Transient field experiments are designed to stop the beam in the target chamber. This is a bad idea when using radioactive beams. The accumulating activity would quickly overwhelm the rate capability of the γ detectors. It is absolutely necessary to devise plans to minimize the buildup of radioactivity in the target chamber.

Depending on the half lives of the activities involved, and often the beams are contaminated by other short lived isotopes, each experiment presents its unique set of challenges.

For the $^{76}$Kr experiment [KUM04] the same experimental setup, including the target, was used as for the stable krypton isotopes' measurements [MER01]. Only, the beam stopper foil was replaced by a moving tape.

The tape solution for the $^{76}$Kr experiment was made possible by the facts that the half life is many hours instead of minutes and that the activity buildup (saturation takes about 4 half lives) takes long compared to the measurement time. The beam is clean. That means there is no contamination from other activities in the beam. The daughter decay products are $^{76}$Br ($T_{1/2}$ = 16.2h) and the stable $^{76}$Se.

The Coulomb-scattered krypton nuclei were stopped in the target backing. For each excited krypton nucleus there are at least 100 elastically scattered nuclei contributing to the activa-

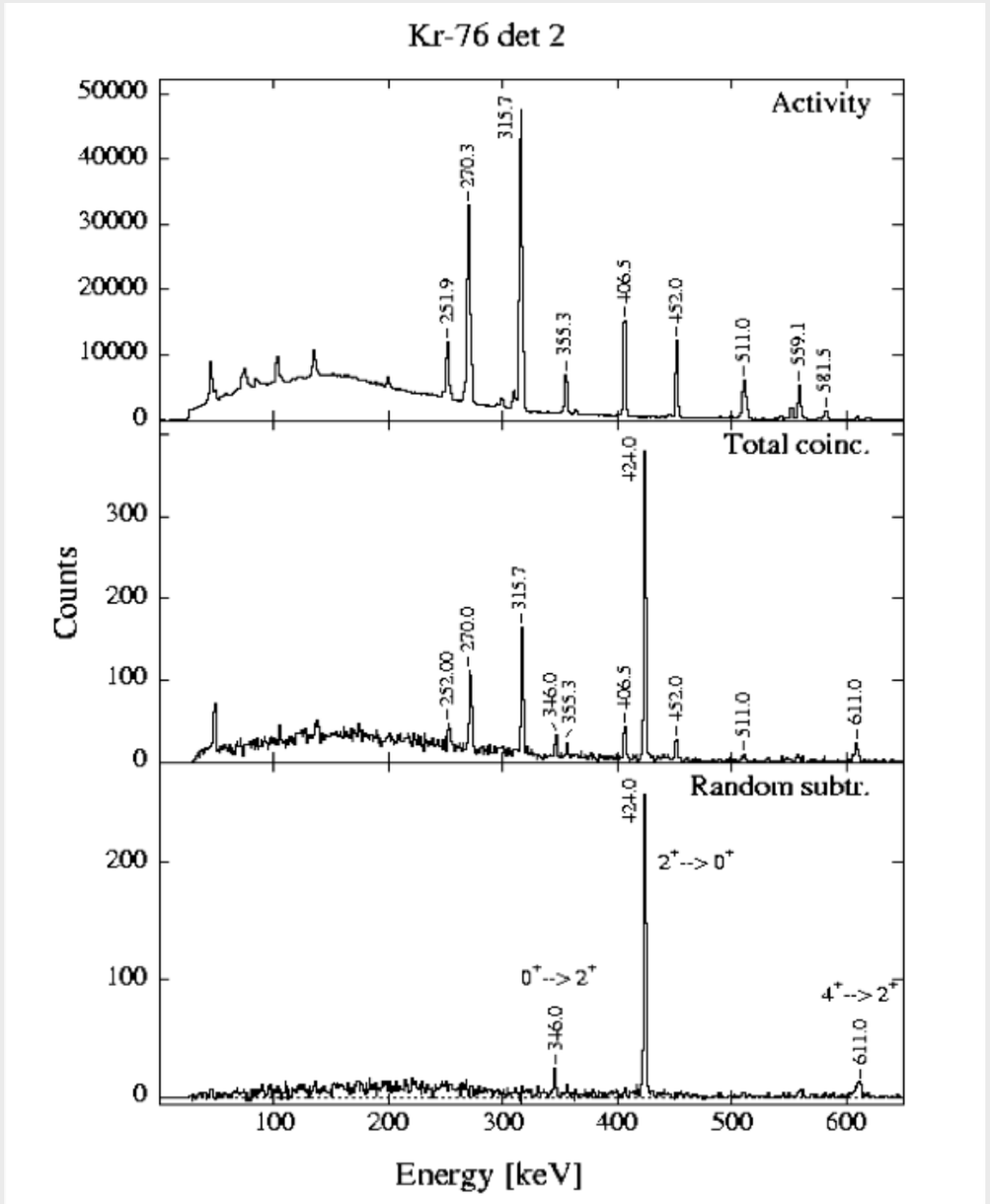


FIGURE 3.3 γ spectra obtained with the $^{76}$Kr beam.

tion of the target. The non interacting beam reached the tape and was moved away.
Since in advance it is usually not known how much beam will be available and for what length of time, when considering a tape to remove the radioactivity, the tape speed needed and limited length of a tape are a major concern. In this case the tape speed could be set to get the activity out fast enough and have the tape last for the duration of the measurement. Actually, it was expected before the experiment that the coincidence requirement is sufficient to extract clean $^{76}$Kr spectra. In figure 3.3 the top spectrum was taken in one clover segment after one production cycle (2 hrs). The singles spectrum was taken for 10 min and shows mainly γ transitions in $^{76}$Br. The total coincidence window was set to 500 ns and the corresponding spectrum is shown in the middle panel. Once the randoms are subtracted indeed only the $^{76}$Kr was left (bottom panel). About 10% of the counts in the $2_1^+ \rightarrow 0_1^+$ peak of $^{76}$Kr are randoms. This number enters into the error calculation and cannot be avoided.

Using the tape method preserved the stopping of the probe ions in the target. This assured the full spin alignment for the precession measurement. To achieve meaningful results the goal should be to collect about 1000 counts per detector and field direction in the γ peak of interest.

# $^{132}$Te: Measurement of g factors of excited states in radioactive beams ....

The utilization of $^{132}$Te as a beam presented new and unique challenges for a transient-field experiment [NBK07]. The half life of $^{132}$Te is $T_{1/2}$ = 3.2 days.

The $^{132}$Te was produced at the Oak Ridge's Holyfield Rare Isotope Facility, an ISOL (Isotope Separation on Line) type of facility. A 50 MeV proton beam induces fission in an uranium target. Fission products are separated, ionized and injected into a tandem accelerator. Because of the magnetic separation the beam is a cocktail of isotopes with the same e/m (charge to mass ratio). In this case roughly 15% of the beam, about $10^6$ particles per second, was $^{132}$Sb with $T_{1/2}$ = 2.79 min. Saturation is achieved within 10 min. But, the really bad news is, that $^{132}$Sb decays into $^{132}$Te and populates the exact same states we want to Coulomb excite. Although the radioactive

FIGURE 3.4 Target chamber for $^{132}$Te experiment

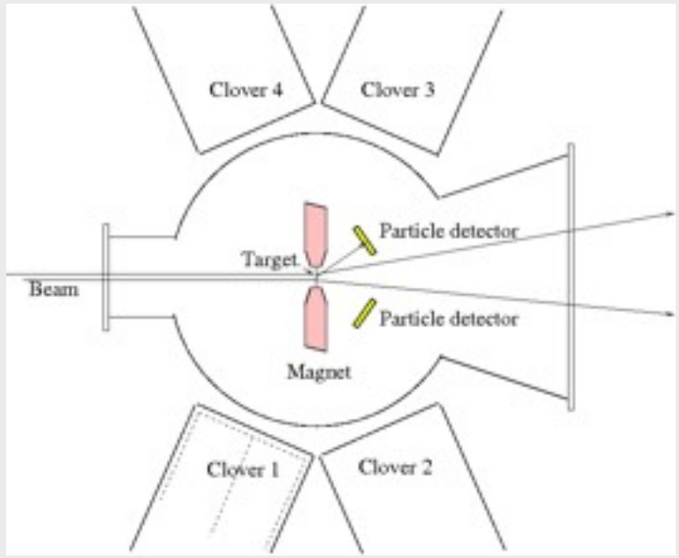


FIGURE 3.5 Layout of chamber.

Magnet and particle detectors shown rotated by 90°. Actual view see below.

The particle detectors are covered by the Cu foils to stop scattered beam particles.

decay is random, it will be much stronger than the Coulomb excitation.

In this case the half life of the contaminant is too short to run a tape.

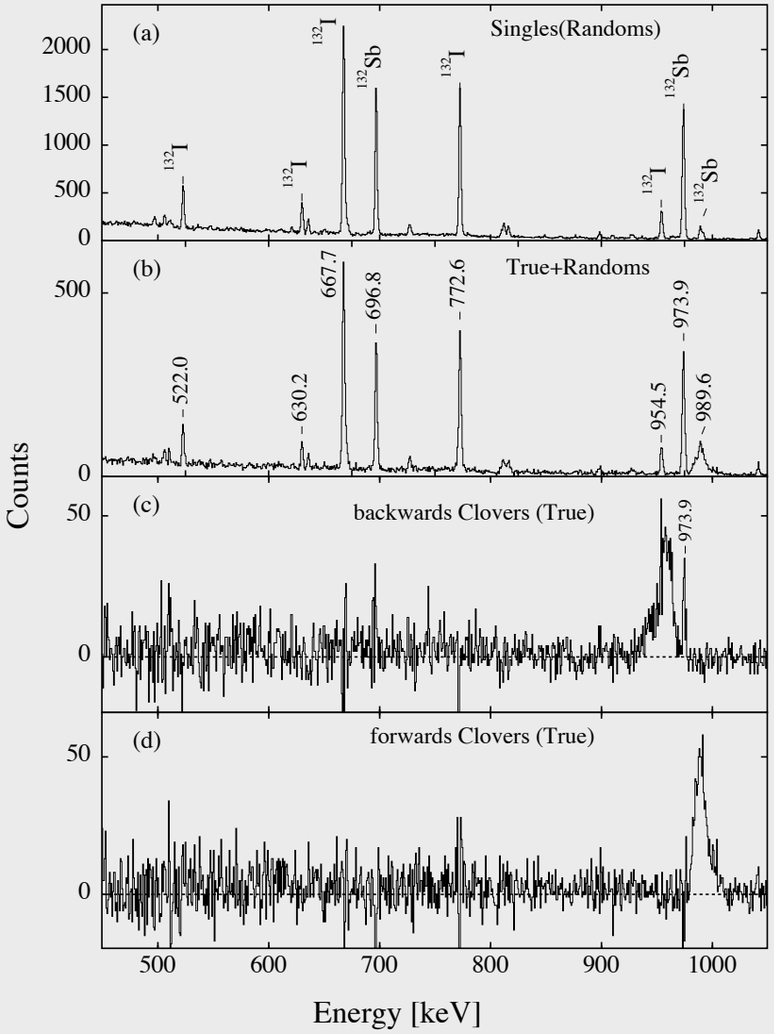


FIGURE 3.6 γ spectra from the $^{132}$Te experiment

The obvious solution was to let the beam pass through the target and out of the chamber into a beam dump downstream away from the γ detectors. The particle detector at zero degrees had to have a center hole to let the beam pass.

Two things had to be considered. A first point of contention was the loss of alignment due to the recoil out of the target because of RIV. And secondly, even a thin target will scatter the beam into a  cone and some particles will unavoidably stop in the chamber and the particle detectors.

The loss of alignment was tested in a special experiment at the Yale Tandem with a stable Te isotope beam at 280 MeV and found to be acceptable for the beam energy. The absolute slope was reduced from 2.4 to 1.6 (30%).

Nevertheless, a first experiment failed because of too high γ rates coming from the target area. In the following experiment the target was reduced to carbon (1.4 mg/cm²), gadolinium (4.9 mg/cm²) and a touch of copper (0.8 mg/cm²), overall some 7 mg/cm².  A new target chamber was used, designed with a wide outlet for the beam and scattered particles. Two quadratic solar devices of 15x15 mm, covering a vertical angle of 19 - 47°, served as particle detector. They were covered with 5.6 mg/cm² copper foils to stop any scattered beam.

These Cu foils at the solar cells still accumulated quite a bit of radioactivity over the course of the experiment (4 days) and were designed to be exchanged if necessary. Another lesson learned was that any obstruction behind the target, like the detector mounts, should be minimized.

But the success of the experiment depended on the fact that the excited probe ions recoiled out of the target.

The decay in flight caused a Doppler shift of the $2_1^+ \rightarrow 0_1^+$ - 973.9 keV transition of more than 13 keV at 67°, enough to separate the full-energy radioactive decay line from $^{132}$Sb and the decay line by the Coulomb excited $^{132}$Te ions from the transient field experiment.

Figure 3.6 contains in (a) a γ-singles spectrum in one of the clover crystals. Dominant are the $4_1^+ \rightarrow 2_1^+ \rightarrow 0_1^+$ transitions in $^{132}$Te, populated by the β decay of $^{132}$Sb at 696.8 keV and 973.9 keV respectively. The lines labeled $^{132}$I stem from the decay of $^{132}$Te and grow slowly as the activation increases.

The second panel (b) shows a γ-coincidence spectrum without randoms subtraction. A broad line at 989.6 keV, which is prompt, can be seen. The two bottom spectra show what is left when the randoms are subtracted. Essentially, the fully Doppler-shifted component from the Coulomb-excited ions is all that is left.

## $^{126}$Sn: Measurement of g factors and mean-life....[KUM122]

The half life of $^{126}$Sn is $T_{1/2}$ = 2.3 x $10^5$ y. For all practical purposes, that can be considered “stable”. Even a good beam stopped in the target will not produce much radioactive decay over the course of an experiment, if it were not for the contamination of the beam by $^{126}$Sb ($T_{1/2}$ = 19 min). Fortunately, the contaminant $^{126}$Sb does not decay into $^{126}$Sn as in the former example.

The $^{126}$Sn beam was also delivered at Oak Ridge National Laboratory at the Holyfield Radioactive Beam Facility. For this experiment, the uranium production target was laced with sulfur. Tin binds with the sulfur while the isobars Sb and Te do not. Extracting SnS molecules from the ISOL target suppressed the Sb

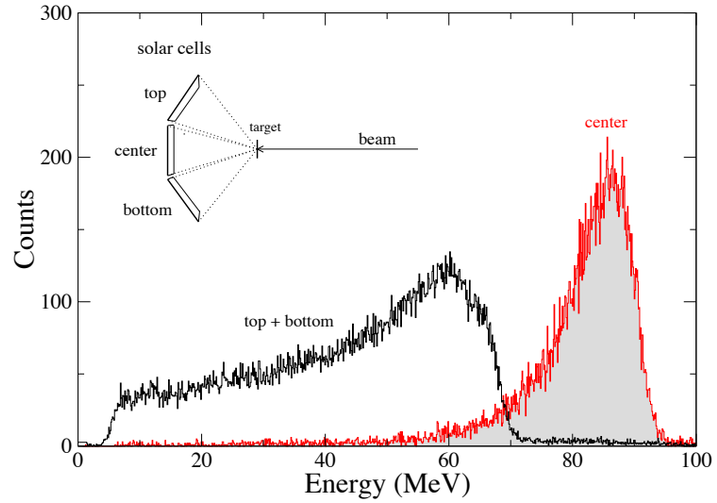


FIGURE 3.7 Coincident C particle spectra

contamination by 4 - 5 orders of magnitude and made it possible to do a conventional transient field experiment. Nevertheless, the beam stopper foil and the thin copper foils in front of the particle detectors were found to be quite “hot” after the run of 3 days.

A triple solar cell array was used as particle detector. The coincident particles are shown in Figure 3.7. Each solar panel was 15 x 15 mm and the total vertical angle covered ±46º.

The particle spectra again tell much about the experiment. In a radioactive beam experiment where the center area has to

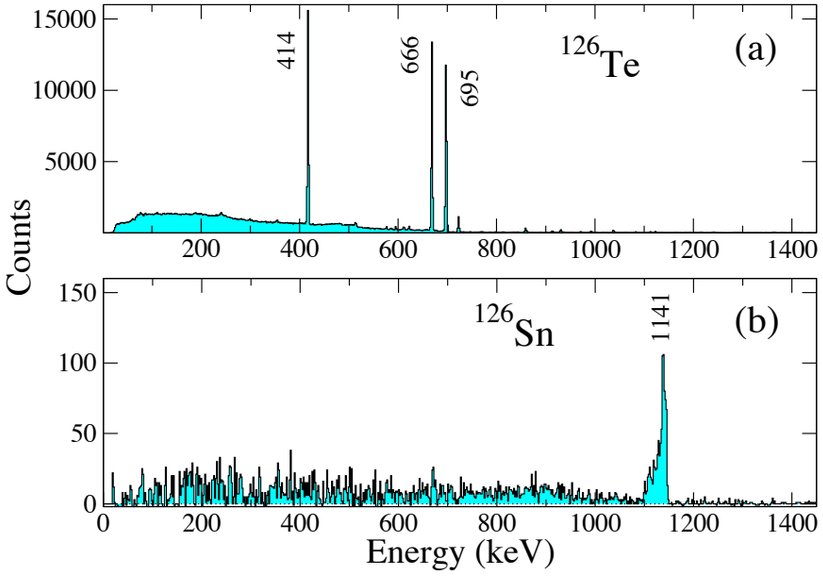


FIGURE 3.8 Gamma spectra. (a) Singles, (b) coincidence spectrum.

be left free, for the beam to pass, a major part of information is lost.

The singles γ spectra were dominated by lines in $^{126}$Te, the end of the β-decay chain, $^{126}$Sn → $^{126}$Sb → $^{126}$Te. Only in the random subtracted coincidence spectrum (Figure 3.8 panel (b)) is the $2_1^+ \rightarrow 0_1^+$ transition in $^{126}$Sn visible.

The *g* factors of the Sn isotope chain were measured in several experiments. Some results lack precision and the agreement between various measurements could be better. A systematic study measuring all stable isotopes in inverse kinemat-

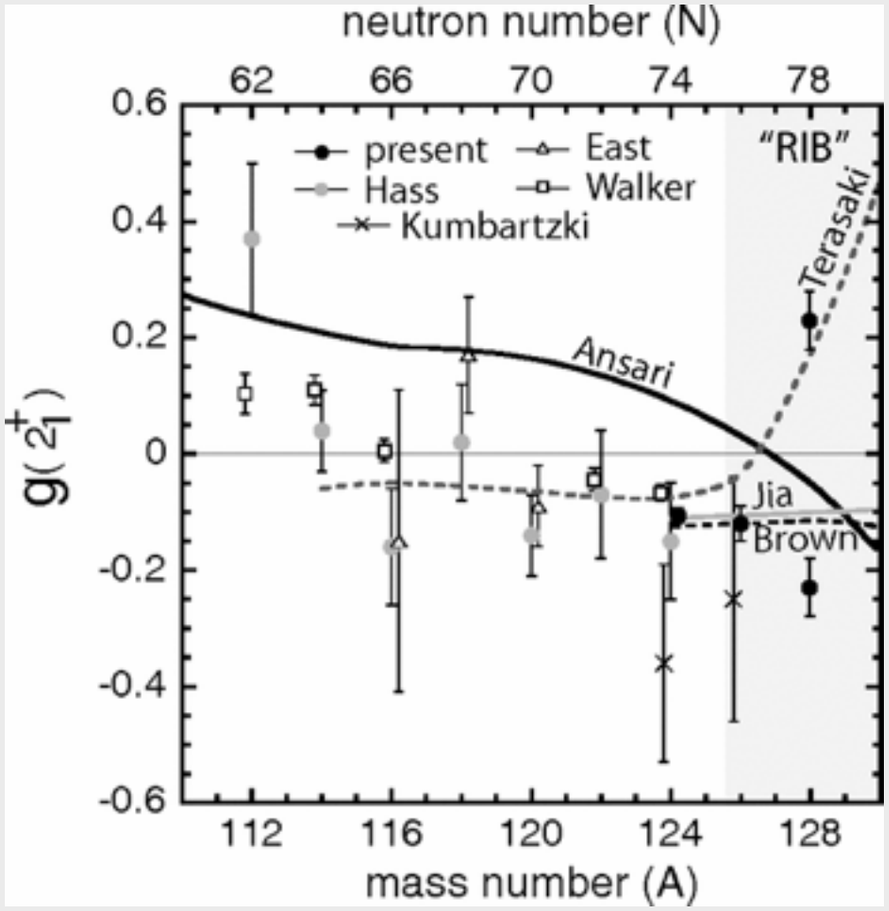


FIGURE 3.9 Compilation of Sn *g* factors taken from a paper by Allmond [AL13].

ics with one target and at energies below the Coulomb barrier has never be done.

The measurements by J.Walker et al. [WA11] claiming the highest precision were all done at energies above the CB, where the Coulomb excitation channel is suppressed and the alignment is not optimal.

For $^{128}$Sn the *g* factor is shown as positive and as negative points, The RIV measurement does not yield the sign of the *g* factor.  A TF measurement is needed to determine the sign.

# Loose Ends

1. **Beam heating and loss of magnetization**
2. **Iron and Gadolinium different?**

### 1. Beam heating.

In Figure 3.10 a correlation of beam intensity and measured precession effect is demonstrated.

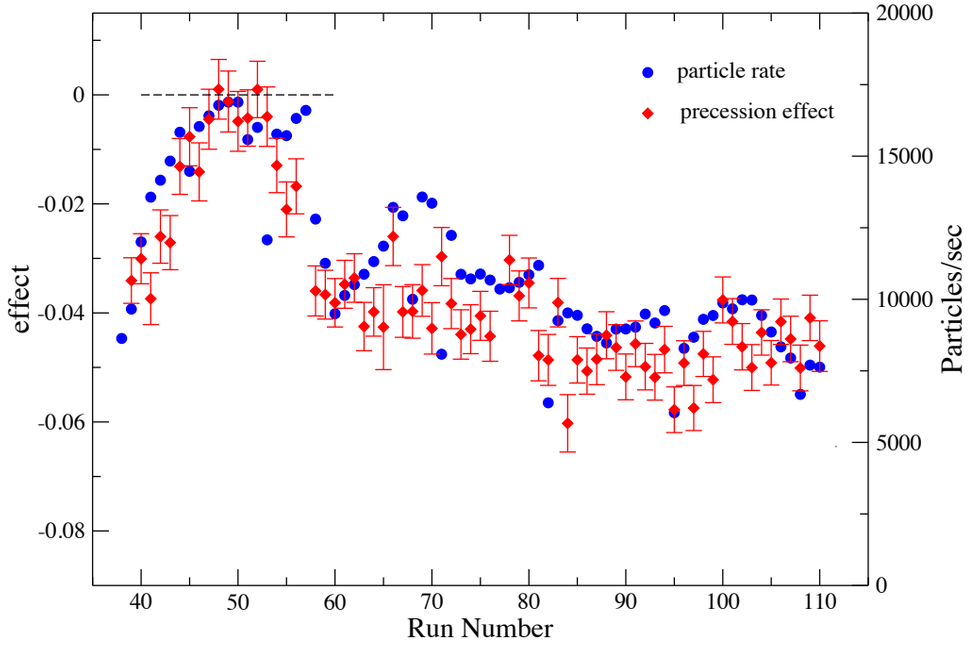


FIGURE 3.10 Correlation between beam intensity and precession results. Each run represents about 1 hr running time. The effect is negative. At high beam currents the effect is zero.

In this example a $^{106}Cd$ beam of 410 MeV, delivered by the Berkeley 88-Inch Cyclotron impinged on a liquid nitrogen cooled multi-layer target: CGdTaCu (0.636, 8.4,1.1, 5.3 mg/cm$^2$ respectively). Forward scattered particles were registered in a particle detector positioned down stream under zero degrees to the beam.

The particle rate (blue dots) is a good measure of the beam current. The precession effect (red dots) should not change since the *g* factor of $^{106}$Cd is a given.

As described before, the transient field strength depends on the magnetization of the ferromagnetic layer which in turn depends on the temperature of the beam spot (see magnetization curve).

Usually it is assumed that in an TF experiment conditions prevail where the offline measured magnetization is preserved. Many published experiment do not even provide a magnetization. The actual beam spot temperature is never known or monitored. Implicitly it is assumed that the temperature of the target is as low as the cooled target frame.

These data set proves otherwise. At sufficiently hight beam intensity, for instance runs 46 - 50, the measured effect is basically zero. The temperature of the beam spot has reached or exceeded the Curie temperature of the ferromagneticum.

The correlation between beam intensity and effect is obvious; lower particle rate - larger negative precession effects.

Since the g factor for the first 2+ state in $^{106}$Cd is known, the precession measurement is indirectly a measurement of the in beam magnetization or beam spot temperature. The data show, the offline measured magnetization of the target of 0.18 T, was reduced in beam to less than 0.15T. It also shows that below a certain beam intensity an “equilibrium” in the magnetization holds.

From this example it has to be concluded that g factor measurements with heavy ion beams at several 100 MeV in inverse kinematics WITHOUT monitoring the target temperature have to be viewed very critical. Very likely, the results tend to be too small (never too large).

The use of iron as ferromagnetic layer therefore should be considered in future experiments. But check the next section.

## 2. Iron versus Gadolinium.

There are only few new measurements done with iron as ferromagnetic material. The most complete data set was taken in May 2011 with the Yale Tandem Accelerator on two targets using $^{106}$Pd as probe ions at beam energies of 240 - 330 MeV (unpublished).

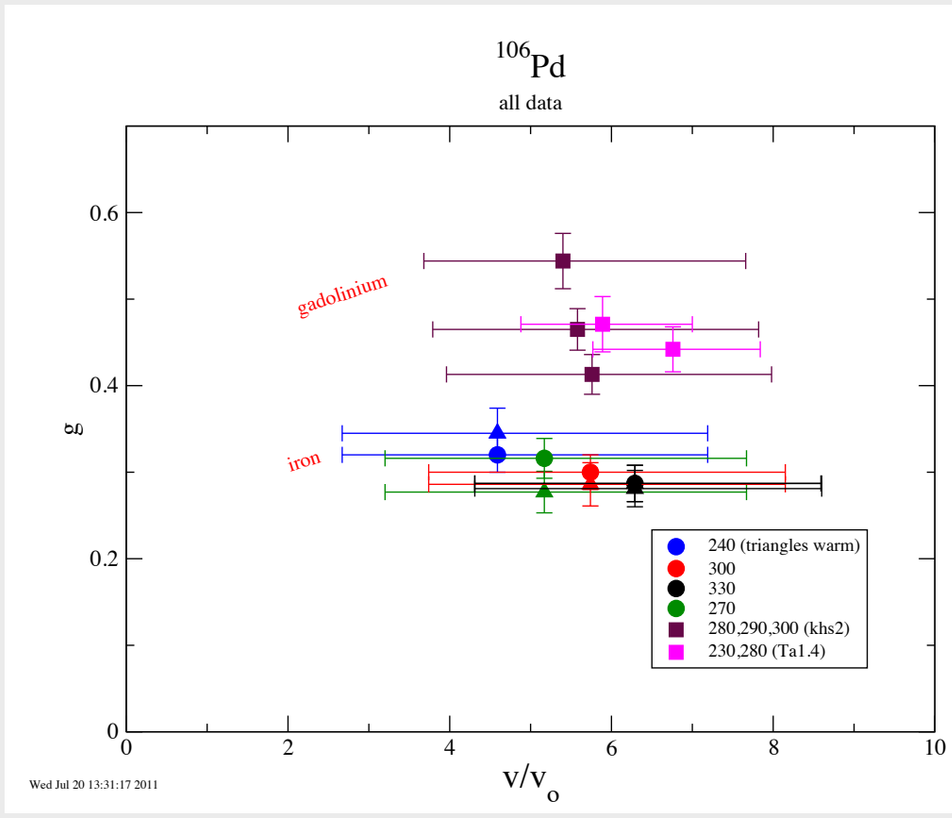


FIGURE 3.11 The adopted g factor of the first $2^+$ state in $^{106}$Pd is 0.40(1).

The results came as total surprise and are shown in Figure 3.11 together with the data taken with gadolinium targets. The data points are calculated with the offline measured magnetization and the Rutgers parametrization (equ.2).

The horizontal “error bars” show the velocity range of the probe ions in the ferromagnetic layer.

The velocity dependence of the parametrization is not observed. In contrast higher velocity points are consistently lower. This could be attributed to a loss of magnetization at higher energies. The iron data were taken at 50 K (circle) and room temperature. The cold data tend to be slightly larger, again in accordance with the temperature dependence of the magnetization.

These data imply either a *g* factor of 0.5 measured with gadolinium or 0.3 for $^{106}$Pd measured with iron. The adopted value is g = 0.40(1), which is considered a standard calibration point.

The striking difference in the iron and gadolinium results is not understood. An immediate control measurement with $^{76}$Ge as beam on the same target and with the same setup reproduced the known *g* factor of $^{76}$Ge as measured with gadolinium targets. No difference between iron and gadolinium here.

This ‘anomaly’ triggered a search for other cases where data from iron and gadolinium  exist. The results are displayed in Figure 3.12.

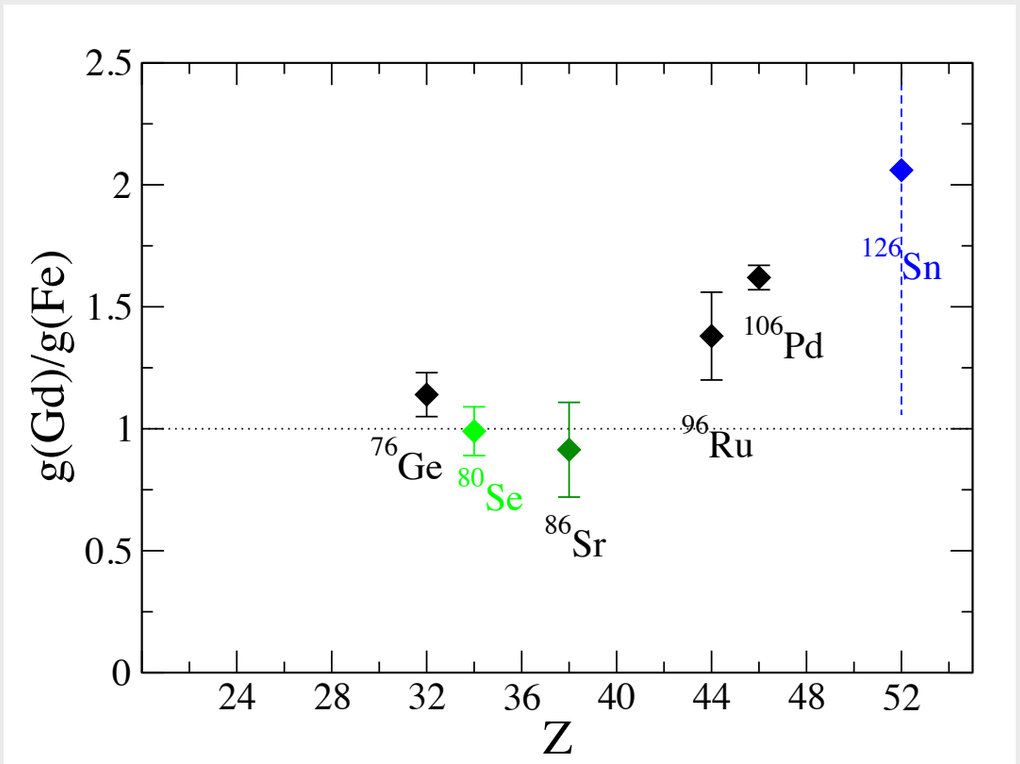


FIGURE 3.12 Ratio of *g* factors measured in inverse kinematics with gadolinium and iron as ferromagneticum..

# Bibliography


AL13 J.M.Allmond, A..Stuchbery et al.,Phys.Rev.C 87, 054325 (2013)

BO68 R.R.Borchers, B.Herskind et al.,Phys.Rev.Lett. 20, 424 (1968)

EB77 J.L.Eberhardt, R.E.Horstman et al., Hyp.Int C 3, 195 (1977)

CBM04 J.R.Cooper, L.Bernstein, M.A.Mahan et al., Nucl. Instr. Methods Phys. Res. A 253, 287 (2004)

HAG96 F.Hagelberg, T,P.Das and K.-H.Speidel, Hyp. Int C 1, 151 (1996)

HOR75 R.F.Horseman, J.L.Eberhart, H.A.Doubt, C.M.E.Otten and G.van Middelkoop, Nucl. Phys. A 248, 291 (1975)

GOL82 G.Goldring in *Heavy Ion Collisions*, editedby R.Bock, North-Holland, Amsterdam (1982) vol. 3, p. 484

KUC88 A.I.Kucharska,J.Billows and M.A.Grace, J.Phys,G 14, 65 (1988)

KUM04 G.Kumbartzki, J.R.Cooper,N.Benczer-Koller et al. Phys.Lett.B 591, 213 (2004)

KUM121 G.J.Kumbartzki et al. Phys.Rev.C 85, 044322 (2012)

KUM122 G.J.Kumbartzki, N.Benczer-Koller, D.A.Torres et al. Phys.Rev.C 86, 034319 (2012)

KUM14 G.J.Kumbartzki, N.Benczer-Koller, S.Burcher et al. Phys.Rev.C 89, 064305 (2014)

LW71 J.Lindhard and A.Winther, Nucl. Phys. **A 116**, 413 (1971)

MA68 J.B.Marion and F.C.Young, Nuclear Reaction Analysis, Graphs and Tables, North Holland (1968)

MER01 T.J.Mertzimekis et al. Phys.Rev.C 64, 024314(2001)

PI89 A.Piquè, J.M.Brennan, R.Darling et al. Nucl.Instrum.Methods Phys.Res A 279, 579 (1989)

RAN73 WL.Randolph et al. Phys. Lett. 44B 36(1973)

SCH37 T.Schmidt, Z. Physik 106, 358 (1937)

SH80 N.K.Shu, D.Melnik, J.M.Brennan,W.Semmler and N.Benczer-Koller, Phys.Rev.C 21, 1828 (1980)

SP89 K.-H.Speidel, M.Knopp, W.Karle et al.,Phys.Lett.B 227, 16 (1989)

STO05 N.J.Stone et al. Phys. Rev.Lett. 94, 192501 (2005)

STU07 A.E.Stuchbery et al. Phys.Rev.C 76, 034306 (2007)
WA11 J.Walker, A.Jungclaus et al., Phys.Rev.C 84, 014319 (2011)
WI66 A.Winther and J.de Boer, Coulomb Excitation, Academic Press, New York

# Review Articles

N.Bencer-Koller and G.J.Kumbartzki, J.Phys.Nucl.Part.Phys.34, R321-R358 (2007)

K.-H.Speidel, O.Kenn and F.Nowacki, Progress in Particle and Nuclear Physics 49, 91 (2002)

N.Benczer-Koller, M.Hass and J.Sak, Annu.Rev.Nucl.Part.Sci. 30, 53 (1980)